

Polarons, localization, and excitonic coherence in superradiance of biological antenna complexes

Meier, Torsten; Zhao, Yang; Chernyak, Vladimir; Mukamel, Shaul

1997

Meier, T., Zhao, Y., Chernyak, V., & Mukamel, S. (1997). Polarons, localization, and excitonic coherence in superradiance of biological antenna complexes. *Journal of Chemical Physics*. 107(10), 3876-3893.

<https://hdl.handle.net/10356/92418>

<https://doi.org/10.1063/1.474746>

© 1997 AIP. This paper was published in *Journal of Chemical Physics* and is made available as an electronic reprint (preprint) with permission of American Institute of Physics. The paper can be found at: [Doi: <http://dx.doi.org/10.1063/1.474746>]. One print or electronic copy may be made for personal use only. Systematic or multiple reproduction, distribution to multiple locations via electronic or other means, duplication of any material in this paper for a fee or for commercial purposes, or modification of the content of the paper is prohibited and is subject to penalties under law.

Downloaded on 23 Aug 2022 22:36:29 SGT

Polarons, localization, and excitonic coherence in superradiance of biological antenna complexes

T. Meier, Y. Zhao, V. Chernyak, and S. Mukamel

*Department of Chemistry and Rochester Theory Center for Optical Science and Engineering,
University of Rochester, Rochester, New York 14627*

(Received 24 February 1997; accepted 3 June 1997)

A real-space formulation of time-resolved fluorescence of molecular aggregates is developed using the one-exciton density matrix $\rho(t)$ of the optically driven system. A direct relationship is established between the superradiance enhancement factor L_s and the exciton coherence size L_p associated with the off-diagonal density matrix elements in the molecular representation. Various factors which affect the latter, including finite temperature, energetic disorder, coupling with phonons, and polaron formation are explored. The theory is applied for the interpretation of recent measurements in the B850 system of the LH2 photosynthetic complexes. © 1997 American Institute of Physics. [S0021-9606(97)50634-9]

I. INTRODUCTION

Optical properties of photosynthetic antenna complexes have become an object of intensive experimental and theoretical studies over the last years.^{1,2} Time and frequency resolved measurements including fluorescence depolarization,^{3,4} hole burning,⁵⁻⁸ pump-probe,⁹⁻¹² and photon echoes^{13,14} provide direct information regarding the dynamics of excitons, energy transfer, and electronic and nuclear relaxation in these systems. In this paper we focus on time-resolved fluorescence and cooperative spontaneous emission (superradiance) which is one of the most interesting elementary signatures of intermolecular coherence. Molecular aggregates are often characterized by ultrafast radiative decays. This effect has a simple classical interpretation: When a collection of dipoles oscillate in phase, their amplitudes add up coherently to form a large effective dipole. The oscillator-strength and consequently the radiative decay rate is then proportional to the number of dipoles. The superradiance coherence size L_s of a molecular aggregate is defined as the ratio of its radiative decay rate to that of a single molecule. (For simplicity we assume in this definition that all molecules are identical and have the same radiative decay rate. This definition can be generalized to aggregates made of different molecules.) The concept of a coherence size was invoked by Mobius and Kuhn¹⁵ in analyzing the dependence of fluorescence quenching on the acceptor surface density for a system consisting of an acceptor monolayer on top of a J-aggregate monolayer. Molecules separated by more than the optical wavelength λ may not emit coherently. $(\lambda/a)^d$ is therefore the fundamental upper bound for L_s ,^{16,17} a being the lattice constant, and d the dimensionality (see Ref. 18 for $d=1$ and Ref. 19 for $d=2$). In practice, however, the coherence size is usually determined by other dephasing mechanisms such as exciton-phonon interactions and static disorder^{18,20-26} and is typically much smaller than both the aggregate physical size and the optical wavelength.^{20,27} Similar types of aggregates can have very different coherence sizes in different environments.²⁸

Recent work on photosynthetic antenna complexes

showed coherence sizes of 2-3 at room temperature, whereas at low temperatures $L_s=3$ for LH2 antenna complexes and $L_s=9$ for LH1.²² Significant decrease of fluorescence lifetimes in J-aggregates of pseudisocyanine (PIC) dyes compared to single chromophores has been observed²⁹ with the fluorescence lifetime varying between 70 ps at 1.5 K to 450 ps at 200 K. PIC J-aggregates are one-dimensional clusters of dye molecules with collective superradiant emission and optical nonlinearities. For example, in PIC-Br J-band, a Strickler-Berg analysis gives the monomer radiative lifetime 3700 ps³⁰ and 70 ps for the aggregate. This implies a superradiance coherence size $L_s=50$ which is much smaller than the number of molecules in the aggregate: $\approx 5 \times 10^4$ obtained from a study of exciton-exciton annihilation.²¹ Coherence sizes of 2-3 were found in mixtures of isocyanine dyes adsorbed on silver halide substrates at room temperature,²⁸ whereas $L_s=70$ has been reported for PIC aggregates in a low temperature glass.²⁷

The finite coherence size L_s in large aggregates is related to the breakdown of translational symmetry of excitons due to static disorder^{18,20,24,25} or to exciton-phonon interactions.²³ In the former case, the coherence size L_s has been attributed to exciton localization length^{18,20,24,25} which exists in one-dimensional systems even for infinitely weak disorder.³¹ Effects of weak disorder on emission of two-dimensional aggregates have been studied using perturbative methods.³² Phonon-induced exciton dephasing has been shown to destroy excitonic coherence and control the superradiance.²³

In this paper we show how the time-resolved fluorescence from aggregates may be calculated and analyzed by exploring exciton dynamics in real-space using the single-exciton density matrix. The superradiance size L_s is shown to be primarily determined by the exciton coherence size L_p . A precise definition of the latter in term of the "anti-diagonal" section of the density matrix is given. We study the effects of static disorder and strong exciton-phonon-coupling on L_p . The density matrix approach further allows us to express the time-resolved fluorescence signal as an overlap of a doorway and a window excitonic wave packets.

The doorway represents the reduced density matrix of the exciton driven by the external pump whereas the window accounts for the system's geometry.

In Sec. II we develop the doorway-window (DW) picture and define the density matrix coherence size L_ρ . The influence of temperature and static disorder on L_ρ in cyclic aggregates is then explored in Sec. III. An additional mechanism for L_ρ resulting from strong exciton-phonon coupling and the formation of polarons is discussed in Sec. IV. A variational calculation of the polaron wave function using Toyozawa's Ansatz allows us to compute the reduced exciton density matrix by tracing the joint (exciton plus phonon) density matrix over the phonon variables. When nuclear motions are slow, we may adopt the simplified adiabatic polaron model commonly used in the description of exciton self-trapping in low-dimensional systems.^{33,34} The DW approach is utilized in Sec. V to calculate the dependence of the superradiance enhancement factor L_s on static disorder, diagonal and off-diagonal exciton-phonon-coupling using the models of Secs. III and IV. Finally in Sec. VI we discuss and summarize our results.

II. REAL-SPACE PICTURE OF TIME-RESOLVED FLUORESCENCE

In this section we develop a real-space description of time-resolved polarized and depolarized fluorescence from molecular aggregates. We show how this signal may be recast in terms of a doorway function which contains all relevant information about the electronic state of the system (expressed through the exciton density matrix), and a window function related to the system's geometry. To set the stage, we introduce a Frenkel-exciton model Hamiltonian which represents an aggregate made out of two-level molecules interacting with a bath consisting of nuclear (intramolecular, intermolecular, and solvent) degrees of freedom:

$$\hat{H} = \sum_n \Omega_n(\mathbf{q}) B_n^\dagger B_n + \sum_{m,n}^{m \neq n} J_{mn}(\mathbf{q}) B_m^\dagger B_n + \hat{H}^{ph}. \quad (1)$$

Here B_n (B_n^\dagger) are exciton annihilation (creation) operators for the n th molecule, \hat{H}^{ph} is the bath (phonon) Hamiltonian, and \mathbf{q} represents the complete set of nuclear coordinates. Exciton-phonon interactions and static disorder are described through the dependence of molecular frequencies Ω_n and the intermolecular couplings J_{mn} on nuclear coordinates \mathbf{q} .

The dipole interaction with the optical field is

$$\hat{H}_{\text{int}} = -\mathbf{E}(t) \cdot \mathbf{P}, \quad (2)$$

where the polarization operator is given by

$$\mathbf{P} = \mu \sum_n U_n(\mathbf{q}) \mathbf{d}_n (B_n + B_n^\dagger). \quad (3)$$

Here $\mu \mathbf{d}_n$ is the transition dipole of the n -th molecule, μ is an average transition dipole and \mathbf{d}_n a dimensionless vector. When all molecular dipole moments are the same, \mathbf{d}_n will be

a unit vector. Otherwise its magnitude will vary with n . $U_n(\mathbf{q})$ are 3×3 orthogonal rotation matrices describing molecular orientations.

The time- and frequency-resolved fluorescence can be related to the dipole-dipole tensor $S^{ij}(\omega, \tau)$:

$$S^{ij}(\omega, \tau) \equiv \frac{\gamma}{\mu^2} \int_{-\infty}^{\infty} dt e^{i\omega t} \left\langle P^i \left(\tau + \frac{t}{2} \right) P^j \left(\tau - \frac{t}{2} \right) \right\rangle, \quad (4)$$

where $\gamma = 4\mu^2 \bar{\omega}^3 / 3\hbar c^3$ is the radiative decay rate of a single molecule with optical frequency $\bar{\omega}$, and the time evolution of $B_n(\tau)$ is given by the molecular Hamiltonian with the external driving field included ($\hat{H} + \hat{H}_{\text{int}}$). Here $i, j = x, y, z$ denote the tensor components of S in a molecular frame. To eliminate propagation and polariton effects which are not essential for the present discussion, we assume that the aggregate's size is much smaller than the optical wavelength.³⁵

The model introduced by Eq. (1) conserves the number of excitons $\mathcal{N} \equiv \sum_n \langle B_n^\dagger B_n \rangle$. If exciton annihilation processes (radiative or nonradiative) are taken into account, \mathcal{N} becomes time-dependent; however, the timescale of \mathcal{N} is typically long compared with exciton equilibration. In either case it is convenient to represent the time-resolved signals as \mathcal{N} times the signal per exciton.

The time-resolved polarized signal $S_n(\tau)$ is given by

$$S_n(\tau) = \gamma \mathcal{N}(\tau) \sum_{i,j=1}^3 \mathcal{P}^{ij}(\tau) n^i n^j, \quad (5)$$

or using operator notation

$$S_n(\tau) = \gamma \mathcal{N}(\tau) \mathbf{n} \cdot \mathcal{P}(\tau) \cdot \mathbf{n}. \quad (6)$$

Here \mathbf{n} is a unit vector denoting the polarization direction of the emitted light, and

$$\begin{aligned} \mathcal{P}^{ij}(\tau) &= [\gamma \mathcal{N}(\tau)]^{-1} \int_{-\infty}^{\infty} \frac{d\omega}{2\pi} S^{ij}(\omega, \tau) \\ &= \frac{1}{\mu^2 \mathcal{N}(\tau)} \langle P^i(\tau) P^j(\tau) \rangle \end{aligned} \quad (7)$$

is the polarization tensor.

The total time- and frequency-resolved fluorescence signal $S(\omega, \tau)$ (summed over directions of polarizations) can be represented in a form

$$\begin{aligned} S(\omega, \tau) &= \frac{\gamma}{\mu^2} \int_{-\infty}^{\infty} dt e^{i\omega t} \left\langle \mathbf{P} \left(\tau + \frac{t}{2} \right) \cdot \mathbf{P} \left(\tau - \frac{t}{2} \right) \right\rangle \\ &= \sum_i S^{ii}(\omega, \tau). \end{aligned} \quad (8)$$

The corresponding time-resolved signal is

$$S(\tau) \equiv \int_{-\infty}^{\infty} \frac{d\omega}{2\pi} S(\omega, \tau) = \gamma \mathcal{N}(\tau) L_s(\tau), \quad (9)$$

where $L_s(\tau)$ is given by the trace of the polarization matrix

$$L_s(\tau) = Tr[\mathcal{A}(\tau)] = \sum_{i=1}^3 \mathcal{P}^{ii}(\tau). \quad (10)$$

We shall now introduce the DW representation for the time-resolved signal $S(\tau)$ by relating $L_s(\tau)$ to the time-dependent doorway (N) and window (M) functions

$$L_s(\tau) \equiv Tr[MN(\tau)] = \sum_{mni} M_{mn}^{ij} N_{mn}^{ij}(\tau), \quad (11)$$

where we use the tensor notation of Eq. (8). M and $N(\tau)$ are thus direct products of $L_0 \times L_0$ matrices in the exciton space (L_0 is the number of molecules) and 3×3 matrices in real space. Hereafter we invoke the rotating-wave approximation for the signal by omitting the terms $\langle B_m B_n \rangle$, $\langle B_m^\dagger B_n^\dagger \rangle$, and $\langle B_m B_n^\dagger \rangle$ occurring in correlation functions of polarization operators in Eqs. (4), (7), and (8). The doorway function $N(\tau)$ is then given by:

$$N_{mn}^{ij}(\tau) \equiv \mathcal{N}^{-1}(\tau) \langle [U_m^\dagger(q) U_n(q)]^{ij} B_m^\dagger B_n \rangle, \quad (12)$$

where the expectation value in the right hand side (r.h.s.) of Eq. (12) is taken with respect to the full density matrix of the system at time τ . The window function is defined by:

$$M_{mn}^{ij} \equiv d_m^i d_n^j. \quad (13)$$

Equations (11), (12), and (13) constitute the DW representation of time-resolved spontaneous light emission. Assuming that the averaging in the r.h.s. of Eq. (12) can be factorized, we obtain

$$N_{mn}^{ij}(\tau) \equiv \mathcal{N}^{-1}(\tau) \langle [U_m^\dagger(q) U_n(q)]^{ij} \rangle \langle B_m^\dagger B_n \rangle. \quad (14)$$

Equation (14) holds in three typical situations: (i) static disorder, when orientational disorder is not correlated with energetic disorder; (ii) weak exciton-phonon-coupling, whereby the full density matrix can be factorized into a product of electronic and equilibrated nuclear parts, which makes the first factor in the r.h.s. of Eq. (14) time independent; (iii) when nuclear motions do not affect dipole orientations.

Neglecting orientational disorder and assuming that all molecules have fixed directions in space, the doorway and window functions become scalars in real space:

$$L_s(\tau) \equiv Tr[MN(\tau)] = \sum_{mn} M_{mn} \rho_{mn}(\tau), \quad (15)$$

with

$$M_{mn} \equiv \mathbf{d}_n \cdot \mathbf{d}_m. \quad (16)$$

The doorway function now coincides with the reduced exciton density matrix:

$$N_{mn}(\tau) = \rho_{mn}(\tau) \equiv \mathcal{N}^{-1}(\tau) \langle B_m^\dagger(\tau) B_n(\tau) \rangle, \quad (17)$$

normalized to a unit trace $Tr[\rho] = \sum_n \rho_{nn} = 1$.

These results can be readily extended to the polarized signal [cf. Eq. (11)]. The DW representation for the polarization matrix becomes

$$\mathcal{P}^{ij}(\tau) = \sum_{mn} \sum_{lk} M_{mn}^{lk} \bar{N}_{mn}^{ij,kl}(\tau), \quad (18)$$

with the window given by Eq. (13), and the doorway

$$\bar{N}_{mn}^{ij,kl}(\tau) \equiv \mathcal{N}^{-1}(\tau) \langle U_m^{il}(q) U_n^{jk}(q) B_m^\dagger B_n \rangle. \quad (19)$$

The doorway function of Eq. (14) is related to the doorway function of Eq. (19) by

$$N_{mn}^{ij}(\tau) = \sum_{k=1}^3 \bar{N}_{mn}^{kk,ij}(\tau). \quad (20)$$

Assuming fixed molecular orientations and neglecting reorientational disorder, the DW representation adopts the form

$$\mathcal{P}^{ij}(\tau) = \sum_{mn} M_{mn}^{ij} \rho_{mn}(\tau), \quad (21)$$

where M_{mn}^{ij} is given by Eq. (13) and ρ_{mn} is the reduced exciton density matrix defined by Eq. (17).

The window function M_{mn} introduced in this section carries all the information regarding dipole orientations necessary for calculating the fluorescence. We note that both M and ρ are $L_0 \times L_0$ Hermitian matrices, L_0 being the number of one-exciton states. They satisfy

$$Tr[\rho] = 1, \quad Tr[M] = f, \quad (22)$$

where f is the total aggregate oscillator strength

$$f \equiv \sum_n f_n, \quad f_n \equiv |\mathbf{d}_n|^2, \quad (23)$$

f_n being the oscillator strength of the n th molecule.

The matrices M_{mn} and ρ_{mn} can be diagonalized using basis sets denoted ϕ_α and Ψ_α , respectively, with $\alpha = 0, 1, \dots, L_0 - 1$. These basis sets are generally different. However, if the aggregate has some symmetry, they may coincide. It is shown in Appendix A that M has no more than three nonzero eigenvalues (superradiant states) denoted by \bar{f}_α , $\alpha = 1, 2, 3$; the corresponding three eigenstates ϕ_α will be hereafter referred to as the superradiant states. We further introduce three orthogonal vectors \mathbf{d}_α which represent the transition dipoles between the ground state and the superradiant states:

$$\mathbf{d}_m = \sum_{\alpha=1}^3 \mathbf{d}_\alpha \phi_\alpha(m), \quad (24)$$

and $\bar{f}_\alpha = |\mathbf{d}_\alpha|^2$. Equation (24) implies that each superradiant state is responsible for the components of all molecular dipoles along one of the orthogonal directions in the laboratory frame; these directions are uniquely determined by the aggregate geometry and are not arbitrary. When all molecular dipoles are in the plane determined by \mathbf{d}_α with $\alpha = 1, 2$ we have $\bar{f}_3 = 0$, while $\bar{f}_2 = \bar{f}_3 = 0$ when all dipoles are oriented along \mathbf{d}_1 . Denoting $\bar{\rho}_\alpha \equiv \langle \phi_\alpha | \rho | \phi_\alpha \rangle$, we obtain for the superradiance factor

$$L_s = \sum_{\alpha=1}^3 \bar{f}_\alpha \bar{\rho}_\alpha, \quad (25)$$

and since $\sum_{\alpha=0}^{L_0-1} \bar{\rho}_\alpha = 1$ we have $L_s \leq \max_\alpha(\bar{f}_\alpha)$, with $\sum_{\alpha=1}^3 \bar{f}_\alpha = f$, which gives an upper bound for the superradiance factor for a given geometry.

The polarization matrix can be also represented in terms of the superradiant states $\phi_\alpha (\alpha=1,2,3)$:

$$\mathcal{P}^{ij} = \sum_{\alpha=1}^3 d_\alpha^i d_\alpha^j \bar{\rho}_\alpha, \quad (26)$$

where d_α^i are components of the superradiant dipole \mathbf{d}_α .

The DW representation of time-resolved spontaneous emission given by Eqs. (15)–(17) will be applied in the coming sections to explore the roles of temperature, disorder and exciton-phonon coupling on the time-resolved fluorescence and superradiance of aggregates. To that end we shall introduce the coherence size L_ρ which characterizes the size of a domain where the molecules emit coherently. Within the approximations adopted here, all information about the state of the system relevant for superradiance is given by the reduced exciton density matrix $\rho_{mn}(\tau)$ whose time dependence reflects the role of relaxation processes on the superradiance factor $L_s(\tau)$. This allows us to introduce a formal definition of the characteristic coherence size L_ρ in terms of the density matrix. By applying the inverse participation ratio concept commonly used in the theory of quantum localization³⁶

$$L_\rho \equiv \left[L_0 \sum_{mn} \left| \rho_{mn} \right|^2 \right]^{-1} \left[\left(\sum_{mn} \left| \rho_{mn} \right| \right)^2 \right]. \quad (27)$$

This quantity gives the length-scale on which the density matrix decays along the ‘‘anti-diagonal’’ direction, i.e., as a function of $n - m$. Similar measures have been successfully used in the analysis of off resonant polarizabilities of aggregates,^{37,38} conjugated polymers,³⁹ and semiconductor nanocrystals.⁴⁰ In the absence of any coherence $\rho_{nm} = L_0^{-1} \delta_{nm}$ and we have $L_\rho = 1$. For a completely coherent distribution $\rho_{nm} = L_0^{-1}$, and $L_\rho = L_0$. If the molecular dipoles are oriented in the same direction, then the superradiance factor is related to the number of molecules in this domain and loss of coherence which leads to the decrease of L_ρ reduces the superradiance. The picture is very different in the opposite situation when the total dipole of an aggregate (i.e., the vector sum of the molecular dipoles) vanishes due to cancellation of contributions from individual molecules. In this case the emission is induced by the loss of coherence, and should increase with the decrease of L_ρ . It is important to note that the size L_ρ depends on the state of the aggregate and is changed when exciton relaxation takes places. This length has only an implicit dependence on the dipole orientation, which comes from the process of preparation of the initially excited state by the exciting optical field. These arguments show that superradiance is a combined effect of aggregate geometry (dipole orientations) and its state, and at least qualitatively all information about the aggregate state relevant for superradiance is contained in the coherence size L_ρ , irrespective of the underlying physical dephasing mechanisms. Superradiance can then be analyzed by first studying the role of different physical mechanisms in affect-

ing the coherence length L_ρ and then relating the superradiance factor L_s to L_ρ and to geometry through the window function.

In the following sections we study various mechanisms which determine the coherence size L_ρ : finite temperatures, disorder-induced localization of excitons, and exciton self-trapping induced by exciton-phonon-coupling. Characteristic sizes associated with these mechanisms will be introduced, and their relations to L_s will be discussed in Sec. V. We shall restrict the following analysis to the case where the exciton equilibration timescale in the excited state manifold is short compared with the radiative decay, and the fluorescence comes from the fully-relaxed exciton density matrix. This case, which always represents the fluorescence at long times, allows us to introduce all the relevant coherence sizes and dephasing mechanisms.

III. TEMPERATURE- AND DISORDER-CONTROL OF EXCITONIC COHERENCE IN CYCLIC AGGREGATES

The ≈ 2.5 Å resolution structure of the LH2 antenna complex of purple bacteria shows two rings: an inner ring (the B850 system) made of 18 chlorophyll molecules and an outer ring (the B800 system) with 9 chlorophylls.⁴¹ Cyclic complexes appear also in other systems such as LH1 which has 32 chlorophylls. All calculations in this article were performed on the B850 system. This aggregate is slightly dimerized and in Appendix B we present the window functions for circular aggregates with two molecules in a unit cell. The values of the coupling J between adjacent chlorophyll molecules in the B850 band used in Ref. 42 are -273 cm⁻¹ and -291 cm⁻¹. However, we do not expect this dimerization to significantly affect the superradiance and for simplicity we have used an average nearest neighbor coupling parameter of $J = -280$ cm⁻¹.

In the absence of disorder, the exciton eigenstates of a ring Ψ_α and their energies ϵ_α are determined by the momenta $k_\alpha = 2\pi\alpha/L_0$, $\alpha = 0, 1, \dots, L_0 - 1$

$$\Psi_\alpha = \frac{1}{\sqrt{L_0}} e^{ik_\alpha m}; \quad \epsilon_\alpha = 2J \cos(k_\alpha). \quad (28)$$

Since J is negative, the $k_0 = 0$ state has the lowest energy.

In this section we shall consider two mechanisms for the loss of excitonic coherence (dephasing): finite temperature, and diagonal energetic disorder. A third mechanism: strong exciton-phonon-coupling resulting in polaron formation will be discussed in the next section.

For weak exciton-phonon-coupling, electronic and nuclear degrees of freedom are decoupled in the equilibrium density matrix (the only role of phonons is then to equilibrate the electronic degrees of freedom), and the reduced exciton density matrix ρ assumes the canonical form:

$$\rho_{\alpha\beta} = \delta_{\alpha\beta} Z^{-1} \exp(-\epsilon_\alpha/T), \quad (29)$$

where we set Boltzmann's constant to 1 and $Z \equiv \sum_\alpha \exp(-\epsilon_\alpha/T)$, ϵ_α were introduced in Eq. (28) and T is

the temperature. In Eq. (29) Greek indices label one-exciton eigenstates Ψ_α with energies ϵ_α . In real-space we have

$$\rho_{mn} = Z^{-1} \sum_{\alpha} \Psi_{\alpha}^{*}(m) \Psi_{\alpha}(n) \exp(-\epsilon_{\alpha}/T). \quad (30)$$

At temperatures lower than the spacing between exciton levels, the aggregate is in the lowest, completely delocalized, exciton state, $\rho_{mn} = L_0^{-1}$ and $L_{\rho} \approx L_0$. As the temperature is raised, higher-momentum excitons become occupied, which decreases L_{ρ} . We define the characteristic thermal size l_T as the size of a cyclic J-aggregate with nearest-neighbor interaction J in which the splitting between the lowest exciton levels is equal to the temperature T

$$l_T^2 = 4\pi^2 |J| T^{-1}. \quad (31)$$

In a translationally-invariant system the density matrix coherence length L_{ρ} is related to l_T . This relation contains a numerical factor which can be calculated using Eq. (30). For example, when the temperature is much smaller than the exciton bandwidth, but much larger than the splitting between the exciton levels at the bottom of the band: $4\pi^2 J/L_0^2 \ll T \ll 4J$, the numerical factor can be evaluated analytically using Eq. (30) and turns out to be close to 1: $L_{\rho} = \sqrt{2/\pi} l_T$.

Disorder can be easily incorporated by averaging Eq. (30) over realizations of disorder using Monte Carlo sampling, resulting in $\langle \rho \rangle$. Static disorder breaks translational symmetry. However, this symmetry is restored upon averaging over disorder, which implies that $\langle \rho \rangle$ becomes diagonal in the momentum representation. The coherence size L_{ρ} is determined by the population of higher-momentum excitons even at low temperatures. Since in one-dimensional systems static disorder leads to localization of exciton states, L_{ρ} can be related to the exciton Anderson localization length l_{ψ} , as can be seen from Eq. (30).

Using these definitions we now discuss the influence of temperature and disorder on the density matrix ρ_{mn} . Figures 1(a)–1(c) show the “anti-diagonal” sections of the density matrices ρ_{mn} calculated using Eq. (30) for different temperatures and disorder strengths. Neglecting disorder and assuming a temperature lower than the splitting between the lowest excitons, only the lowest exciton is populated in thermal equilibrium. Due to the symmetry, the corresponding density matrix will be delocalized over the entire ring, and L_{ρ} will be equal to the system size $L_0 = 18$.

With increasing temperature, higher exciton states are populated and ρ becomes more localized. This effect is shown in Fig. 1(a), where the canonical density matrices for temperatures 50 K (solid), 100 K (dashed), and 300 K (dotted) are displayed. The temperature-induced localization can be clearly seen. The corresponding values of L_{ρ} are 14.6, 10.5, and 5.95, respectively. In the high temperature limit all exciton states are equally populated and the density matrix becomes completely localized (diagonal) resulting in $L_{\rho} = 1$.

Figure 1(b) illustrates how disorder leads to localization of the density matrix at low temperatures. Energetic diagonal disorder has been included by assuming that Ω_n have inde-

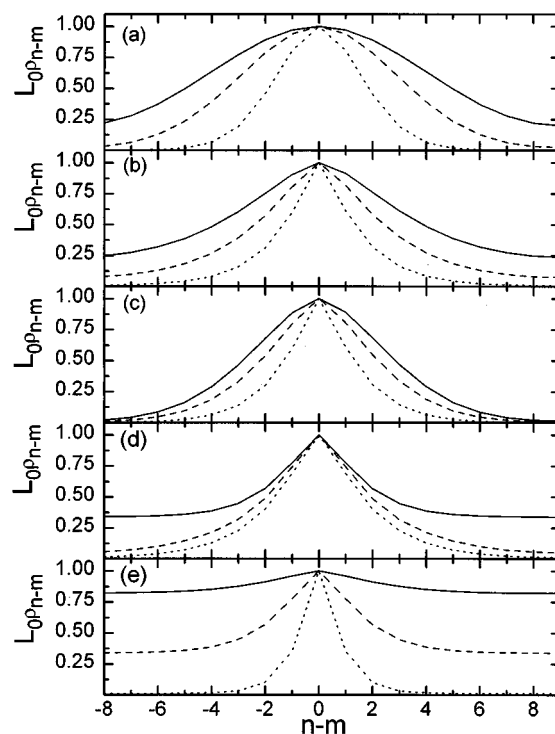


FIG. 1. Thermally relaxed density matrices. (a) Purely exciton systems (no disorder and phonons), for different temperatures, solid: 50 K, $L_{\rho} = 14.55$; dashed: 100 K, $L_{\rho} = 10.47$; dotted: 300 K, $L_{\rho} = 5.95$. (b) For different disorder strengths at 4 K, solid: 330 cm^{-1} , $L_{\rho} = 14.55$; dashed: 565 cm^{-1} , $L_{\rho} = 10.64$; dotted: 1130 cm^{-1} , $L_{\rho} = 6.16$. (c) For different disorder strengths at 100 K, solid: 330 cm^{-1} , $L_{\rho} = 9.40$; dashed: 565 cm^{-1} , $L_{\rho} = 8.044$; dotted: 1130 cm^{-1} , $L_{\rho} = 5.53$. (d) Diagonal exciton-phonon coupling, $J_R = 8$, $\kappa = 0.5$ and three reduced temperatures, solid: $T_R = 10^{-3}$, $L_{\rho} = 15.5$; dashed: $T_R = 0.1$, $L_{\rho} = 9.58$; dotted: $T_R = 0.2$, $L_{\rho} = 7.26$. (e) Diagonal exciton-phonon coupling, $T_R = 10^{-3}$, $J_R = 8$ and three values of κ , solid: $\kappa = 0.125$, $L_{\rho} = 17.9$; dashed: $\kappa = 0.5$, $L_{\rho} = 15.5$; dotted: $\kappa = 0.781$, $L_{\rho} = 3.52$.

pendent Gaussian distributions with the same mean $\bar{\Omega}$ (independent of n) and FWHM σ . Calculations were made using a Monte Carlo sampling over different realizations. As shown in Fig. 1(b), this localization becomes stronger with increasing σ . The corresponding values of L_{ρ} at 4 K are 14.6, 10.6, and 6.16 for $\sigma = 330 \text{ cm}^{-1}$, 565 cm^{-1} , and 1130 cm^{-1} , respectively. In the limit of very strong disorder the density matrix becomes completely localized (diagonal) and we have $L_{\rho} = 1$. The combined influence of disorder and temperature is illustrated in Fig. 1(c) where equilibrium density matrices are shown at $T = 100 \text{ K}$ for different values of σ . The values of L_{ρ} at 100 K are 9.40, 8.04, and 5.53 for $\sigma = 330 \text{ cm}^{-1}$, 565 cm^{-1} , and 1130 cm^{-1} , respectively. The density matrices become more localized with increasing disorder and temperature, as is evident by comparing Fig. 1(c) with Fig. 1(b).

IV. POLARON CONTROL OF EXCITONIC COHERENCE

When exciton-phonon-coupling is weak, the phonon degrees of freedom may be eliminated and their effects incorporated through relaxation superoperators calculated perturbatively in the exciton-phonon-coupling strength.^{43,44} The

detailed-balance condition satisfied by the relaxation super-operator guarantees that at long times the system evolves into a thermal distribution of bare excitons. The corresponding coherence size L_ρ then does not depend on the nature of the phonons and their coupling with excitons. The analysis of equilibrated excitons in Sec. III therefore implicitly assumes weak exciton-phonon coupling. This state of affairs changes drastically as the coupling strength is increased. In this section we consider the effects of strong exciton-phonon-coupling on the coherence size. It is shown in Appendix C how higher order effects of exciton-phonon coupling on the reduced exciton density matrix ρ_{mn} can be taken into account perturbatively. The following analysis is non-perturbative and is based on the polaron model.³³

We adopt the Hamiltonian Eq. (1) with the Einstein phonon Hamiltonian \hat{H}^{ph} ,

$$\hat{H}^{ph} = \sum_n \hbar \omega_0 b_n^\dagger b_n, \quad (32)$$

where b_n^\dagger creates a phonon of frequency ω_0 on site n , and we have one Einstein oscillator per molecule. Exciton-phonon interactions enter through the nuclear coordinate influence on both molecular frequencies (diagonal coupling) and intermolecular interactions (off-diagonal coupling). Expanding $\Omega_n(\mathbf{q})$ to first order in phonon coordinate \mathbf{q} , the first term of Eq. (1) reads

$$\sum_n \Omega_n(\mathbf{q}) B_n^\dagger B_n = \sum_n \Omega_n(\mathbf{q}=0) B_n^\dagger B_n + \hat{H}^{diag}, \quad (33)$$

with the diagonal exciton-phonon-coupling term

$$\hat{H}^{diag} = g \hbar \omega_0 \sum_n B_n^\dagger B_n (b_n^\dagger + b_n), \quad (34)$$

and g is a dimensionless diagonal coupling constant.

Expanding $J_{mn}(\mathbf{q})$ to first order in phonon coordinates, we write the second term of Eq. (1) as

$$\sum_{m,n}^{m \neq n} J_{mn}(\mathbf{q}) B_m^\dagger B_n = \sum_{m,n}^{m \neq n} J_{mn}(\mathbf{q}=0) B_m^\dagger B_n + \hat{H}^{o.d.} \quad (35)$$

with the off-diagonal coupling term^{45,46}

$$\begin{aligned} \hat{H}^{o.d.} = & \frac{\phi}{2} \hbar \omega_0 \sum_{nl} [B_n^\dagger B_{n+1} (b_l^\dagger + b_l) (\delta_{n+1,l} - \delta_{nl}) \\ & + B_n^\dagger B_{n-1} (b_l^\dagger + b_l) (\delta_{nl} - \delta_{n-1,l})]. \end{aligned} \quad (36)$$

The second term of (36) is the Hermitian conjugate of the first. Here we have assumed nearest-neighbor coupling, and ϕ is a dimensionless parameter controlling the off-diagonal coupling strength. Equation (34) and Eq. (36), together with \hat{H}^{ph} and the zeroth-order intermolecular coupling term, result in the generalized Holstein Hamiltonian \hat{H}^{GH} (the original Holstein Hamiltonian contains diagonal coupling only).³⁴

$$\begin{aligned} \hat{H}^{GH} = & \sum_n \Omega_n(\mathbf{q}=0) B_n^\dagger B_n + \sum_{m,n}^{m \neq n} J_{mn}(\mathbf{q}=0) B_m^\dagger B_n + \hat{H}^{ph} \\ & + \hat{H}^{diag} + \hat{H}^{o.d.} \end{aligned} \quad (37)$$

There are two competing energy scales in the Holstein Hamiltonian, namely, the lattice relaxation energy $g^2 \omega_0$ and the bare exciton bandwidth $4J$. Their ratio will be denoted the coupling strength

$$\kappa = g^2 \omega_0 / 4J \quad (38)$$

which determines the size of the polaron as well as exciton-phonon correlations. In typical molecular crystals, $g^2 \lesssim 1$, in ionic crystals g^2 is large compared to unity, and in semiconductors g^2 is between the former two. In anthracene, for example, κ is about 0.4, and in pyrene, about 0.8~1.6.⁴⁷ The other two important parameters of the model are the reduced bandwidth (the ratio between the bare exciton bandwidth $4J$ and the characteristic phonon frequency ω_0)

$$J_R = 4J / \omega_0, \quad (39)$$

and the reduced temperature

$$T_R = T / \omega_0. \quad (40)$$

For strong exciton-phonon-coupling ($\kappa \gg 1$), solutions of the Holstein Hamiltonian are known as small polarons because the exciton-induced lattice distortion is confined to essentially a single exciton site.⁴⁸ For weak exciton-phonon coupling ($\kappa \ll 1$), the spatial extent of the lattice distortion is significantly increased and the resulting phonon-dressed exciton is called a large polaron. The crossover from a large polaron to a small polaron with increasing exciton-phonon coupling (often called the self-trapping transition) is rather abrupt for large intermolecular coupling J . In the limit of slow lattice motions ($J_R \gg 1$), adiabatic polaron theories admit approximate solutions in the form of solitons.

The off-diagonal coupling in Eq. (36) has positive (negative) signs for electronic transfer to the left (right) of the distorted lattice site. While exact solutions exist for diagonal coupling in the $J_R \rightarrow 0$ limit (the small polaron), the Hamiltonian with off-diagonal coupling has not been diagonalized analytically. Adding intermolecular interactions and diagonal coupling complicates the problem even further. Due to difficulties in obtaining simple solutions,⁴⁹ off-diagonal coupling is less frequently used compared with its diagonal counterpart.

To calculate ρ_{mn} we assume that exciton-phonon coupling leads to the formation of bands of collective exciton-phonon states, and the many-body polaron wave function is given by the Toyozawa Ansatz⁵⁰ (see Appendix D):

$$|K\rangle = L_0^{-1} \sum_n e^{iKn} |\Lambda_n^K\rangle \sum_m \psi_{m-n}^K B_m^\dagger |0\rangle_{ex}. \quad (41)$$

Here $|K\rangle$ is the lowest polaron state with momentum K , $|0\rangle_{ex}$ is the exciton vacuum state, and $|\Lambda_n^K\rangle$ are phonon wave functions centered at site n containing a coherent state on each site l with a displacement λ_l^K [cf. Eq. (D6)]. $|\Lambda_n^K\rangle$ is different from $|\Lambda_{n'}^K\rangle$ only by a shift of $n - n'$ lattice con-

stants. The parameters λ_l^K , ψ_l^K , and the polaron energy band E_K , are obtained variationally. The phonon wave functions $|\Lambda_n^K\rangle$ represent a lattice distortion forming a potential well centered at n and trapping the exciton with an amplitude distribution of ψ_l^K .

At sufficiently low temperatures ($T_R \ll 1$), only the lowest polaron band is populated, and the many-body exciton-phonon density matrix ρ_M is given by

$$\rho_M = Z^{-1} \sum_K \langle K|K\rangle^{-1} |K\rangle e^{-E_K/T} \langle K|, \quad (42)$$

where E_K are the polaron energies and $Z \equiv \sum_K \exp(-E_K/T)$ is the partition function.

It should be emphasized that the polaron state is delocalized over the entire aggregate even though both exciton amplitudes ψ_l^K and phonon displacements λ_l^K are localized. We shall demonstrate that the size of ψ_l^K , hereafter referred to as the polaron size l_p , which can be formally defined by $l_p \equiv 1/|\sum_l \psi_l^K|^4$, shows up as the localization length of ρ_{mn} (i.e., as the coherence size L_ρ). l_p can therefore be directly observed in superradiance measurements. To that end we substitute Eqs. (42) and (41) into $\rho_{mm'} = \text{Tr}(\rho_M B_m^\dagger B_{m'})$ yielding

$$\rho_{mm'} = L_0^{-2} \sum_K \langle K|K\rangle^{-1} e^{-E_K/T} \times \sum_{nn'} e^{iK(n'-n)} \psi_{m-n}^K \psi_{m'-n'}^{K*} F_{n'n}^K, \quad (43)$$

with the Debye-Waller factor

$$F_{n'n}^K \equiv \langle \Lambda_{n'}^K | \Lambda_n^K \rangle = \exp \left[L_0^{-1} \sum_q |\lambda_q^K|^2 (e^{iq(n-n')} - 1) \right], \quad (44)$$

and λ_q^K is the Fourier transform of λ_n^K (see Appendix D):

$$\lambda_q^K = \sum_n e^{-iqn} \lambda_n^K. \quad (45)$$

Localization of $\rho_{mm'}$ is determined by the combined effect of electronic confinement (that of ψ_{m-n}^K) and the nuclear factor $F_{n'n}^K$ which represents the overlap (scalar product) $\langle \Lambda_{n'}^K | \Lambda_n^K \rangle$ of two coherent states.

The reduced density matrix ρ_{m-n} is shown in Fig. 1(d) for $J_R=8$, $\kappa=0.5$ and three reduced temperatures $T_R=10^{-3}$, 0.1, 0.2. L_ρ for the three reduced temperatures are 15.5, 9.58, and 7.26, respectively. Comparison with the other panels shows that at finite temperatures, polaron-induced and disorder-induced localization of ρ_{m-n} are very similar. At zero temperature, only the $K=0$ polaron state is populated, and the reduced density matrix becomes

$$\rho_{mm'} \propto \sum_{nn'} \psi_{m-n}^{K=0} \psi_{m'-n'}^{K=0*} \langle \Lambda_{n'}^{K=0} | \Lambda_n^{K=0} \rangle. \quad (46)$$

In Fig. 1(e), we display the reduced density matrix ρ_{m-n} for $T_R=10^{-3}$, $J_R=8$, and $\kappa=0.125$, 0.5 and 0.78. The corresponding L_ρ are 17.9, 15.5, and 3.52, respectively. ρ_{m-n} has a constant finite component at large $|m-n|$ in addition to the

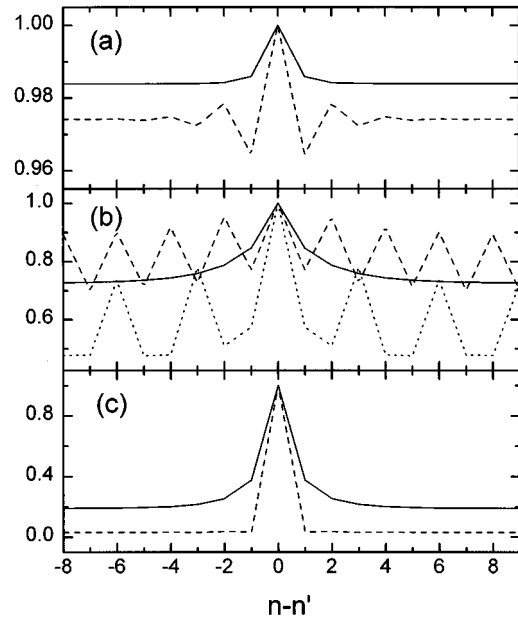


FIG. 2. The Debye-Waller factor $F_{n'n}^K$. (a) Weak coupling, $\kappa=0.0125$, narrow band, $J_R=0.8$, two crystal momenta are shown: $K=0$ (solid) and $K=\pi$ (dashed); (b) weak coupling, $\kappa=0.125$, broad band, $J_R=8$, three crystal momenta are shown: $K=0$ (solid), $K=\pi$ (dashed) and $K=2/3\pi$ (dotted); (c) intermediate coupling, $\kappa=0.5$, $J_R=8$, two crystal momenta are selected: $K=0$ (solid) and $K=\pi$ (dashed).

polaron-induced localized structure at small $|m-n|$. To trace the origin of this behavior, let us examine more carefully the Debye-Waller factor. $F_{n'n}^K$ decreases from 1 at $n=n'$ to a constant at large $|n-n'|$ over a characteristic lengthscale which will be denoted by l_{DW} . A formal definition of l_{DW} can be obtained by subtracting its value \bar{F} for large $|n-n'|$ and substituting $F_{n'n}^K - \bar{F}$ into Eq. (27) instead of ρ_{mn} . The Debye-Waller factor can be recast in the form

$$F_{n'n}^K = \exp(\sigma_{n-n'}^K - \sigma_0^K), \quad (47)$$

where $\sigma_{n-n'}^K$ is the Fourier transform of $|\lambda_q^K|^2$. Because $\sigma_{n-n'}^K$ decays rapidly to zero with increasing $|n-n'|$, the Debye-Waller factor $\langle \Lambda_{n'}^K | \Lambda_n^K \rangle$ at large $|n-n'|$ equals $\exp(-\sigma_0^K)$ which becomes $\exp(-g^2)$ in the $J_R \rightarrow 0$ limit.

In Fig. 2, the Debye-Waller factor $\langle \Lambda_{n'}^K | \Lambda_n^K \rangle$ is displayed as a function of $n-n'$ for different polaron momenta K . Two weak-coupling cases are shown, $\kappa=0.0125$, $J_R=0.8$ ($J_R < 1$, narrow band) and $\kappa=0.125$, $J_R=8$ ($J_R > 1$, broadband). For the first case, $F_{n'n}^K$ hardly deviates from 1 for both $K=0$ and $K=\pi$, as shown in Fig. 2(a). For the second case, the Debye-Waller factor reflects the one-phonon plane-wave of high momentum states. For $J_R=8$, $\kappa=0.5$, the Debye-Waller factor has a constant component $\exp(-\sigma_0^K)$ which decreases with increasing crystal momentum as is evident from comparing the two crystal momenta, $K=\pi$ and $K=2/3\pi$, displayed in Fig. 2(c). For intermediate to strong couplings, it is safe to assume that the Debye-Waller factor size l_{DW} is much smaller than l_p . This implies that only those terms with $|n-n'| \leq l_p$ contributes to Eq. (43), and since ψ_l^K has a size of l_p the reduced density matrix is localized on the l_p

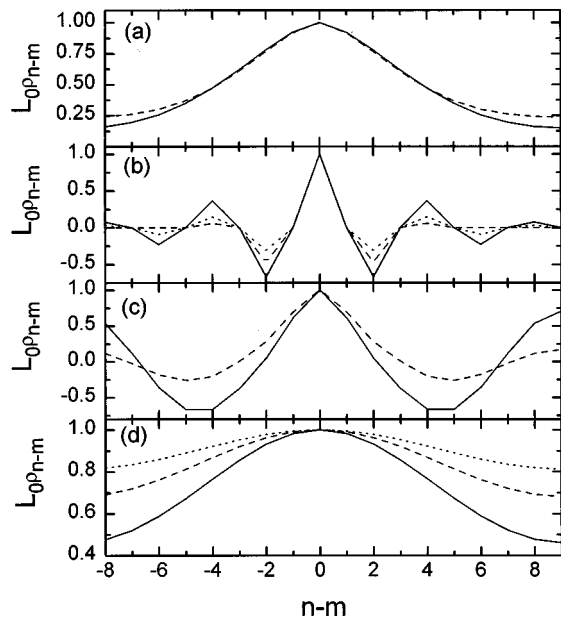


FIG. 3. Reduced exciton density matrices for the polaron model. (a) For two reduced temperatures $T_R=0.27$ (solid, $L_\rho=13.24$), and $T_R=0.49$ (dashed, $L_\rho=14.27$), $J_R=8, \kappa=0.125$. The corresponding polaron band is shown in Fig. 4(a). (b) For two temperatures $T_R=0$ (solid, $L_\rho=5.95$) and $T_R=0.2$ (dotted, $L_\rho=2.93$), $\phi=1, J_R=g=0$. Also shown for comparison is the reduced density matrix for $\phi=g=1, J_R=T_R=0$ (dashed, $L_\rho=3.71$). The corresponding polaron band is shown in Fig. 4(b). (c) $\phi=1, J_R=2$ and $T_R=10^{-3}$ (solid, $L_\rho=13.9$), $T_R=10^{-2}$ (dashed, $L_\rho=8.9$). The corresponding polaron band is shown in Fig. 4(c). (d) For soliton profiles [Eqs. (48) and (50)] for three strengths of nonlinearity: $a_0=3$ (solid), $a_0=4$ (dashed) and $a_0=5$ (dotted). $L_\rho=17.9, 17.7$, and 16.8 , respectively.

lengthscale as a function of $|n-n'|$. The constant component of the reduced density matrix ρ_{m-n} for large $n-m$ shown in Fig. 1(d) reflects the similar behavior of the Debye-Waller factor.

In the weak coupling ($\kappa \ll 1$) limit of the broadband ($J_R > 1$) case, the Debye-Waller factor Eq. (44) for high crystal momentum states has a one-phonon plane-wave component due to strong interactions with the one-phonon scattering continuum, as shown in Fig. 2(b). As a result, for some temperature range, $\rho_{mm'}$ may become more delocalized at higher temperatures. This counterintuitive behavior is related to the increase in population of higher-momentum states which have the one-phonon plane-wave as the phonon wave function, as the temperature is raised. As shown in Fig. 3(a), $\rho_{mm'}$ at $T_R=0.49$ has a longer off-diagonal tail than $\rho_{mm'}$ at $T_R=0.27$. For small $|m-m'|$, though, $\rho_{mm'}$ at $T_R=0.49$ remains slightly more localized than $\rho_{mm'}$ at $T_R=0.27$. L_ρ for the two cases are 14.27 and 13.24, respectively. Figure 4(a) shows the corresponding polaron band. The flat regions of the polaron band at higher crystal momenta are responsible for the counterintuitive behavior of the reduced exciton density matrix shown in Fig. 3(a).

In summary, we have shown that in the absence of static disorder and at low temperatures, the coherence size L_ρ is related to the characteristic sizes l_p and l_{DW} , even though the excitons are not localized, in contrast to the case of static disorder. The polaron size l_p reflects the size of the trapped

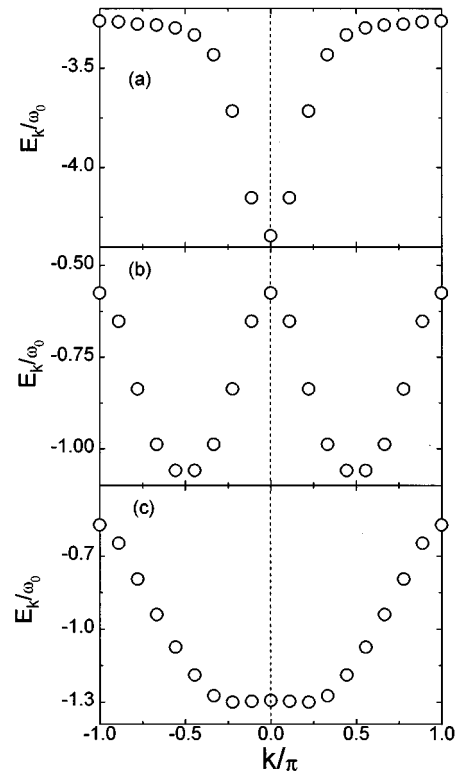


FIG. 4. Dispersion curves (E_K vs K) for the lowest polaron band. (a) Diagonal coupling only, $J_R=8, \kappa=0.125$. (b) Diagonal and off-diagonal coupling, $J_R=0, \phi=g=1$. (c) Off-diagonal coupling only, $\phi=1, J_R=2$.

exciton wave function, whereas l_{DW} shows a typical separation between the traps related to the left (bra) and right (ket) components of the density matrix. The coherence size depends on both l_p and l_{DW} , however when $l_{DW} \ll l_p$ the length l_{DW} is irrelevant. The constant tail \bar{F} of $F_{nn'}$, which does not vanish at large values of $|n-n'|$ may be important in large aggregates and at low temperatures. Representing the Debye-Waller factor as $F_{mn} = (F_{mn} - \bar{F}) + \bar{F}$ in Eq. (43) we recast the density matrix $\rho_{mm'}$ in a form $\rho_{mm'} = \rho_{mm'}^{(0)} + \rho_{mm'}^{(1)}$. By substituting $\rho_{mm'}^{(0)}$ and $\rho_{mm'}^{(1)}$ into Eq. (27) we obtain L_ρ which saturates and scales like L_0 , respectively, for large L_0 . Since in the case of strong and intermediate coupling \bar{F} is usually small at intermediate sizes L_0 , L_ρ does not depend on L_0 while at large L_0 we have $L_\rho \propto L_0$. The size l_c which determines the crossover region can be defined as the value of L_0 when contributions of $\rho_{mm'}^{(0)}$ and $\rho_{mm'}^{(1)}$ are equal. The smaller \bar{F} , the larger is l_c .

We now turn to off-diagonal coupling. LH2 has significant dipole-dipole interactions up to the third neighbor.⁴² It is reasonable to assume that these interactions are affected by various phonon modes. The two sets of variational parameters ψ_l and λ_l of the Toyozawa Ansatz provide an adequate description of off-diagonal coupling as well, and the resulting exciton-phonon correlations and polaron energy bands compare favorably with the Munn-Silbey approach at zero temperature.^{45,46}

In Fig. 3(b) we show the influence of off-diagonal cou-

pling on the reduced density matrix ρ_{mn} . For $J_R = g = 0$ (off-diagonal coupling only), the polaron band is symmetric with respect to $K = \pm \pi/2$ as demonstrated in Fig. 4(b). As a result, ρ_{m-n} vanishes for odd $m-n$. For even $m-n$, ρ_{m-n} has alternating signs reflecting the dynamic dimerization introduced by off-diagonal coupling. Increase in temperature reduces the amplitudes of ρ_{m-n} at nonzero even $m-n$. Diagonal coupling has a similar effect on ρ_{m-n} as the temperature, i.e., it suppresses ρ_{m-n} for nonzero even $m-n$. However, as is evident from Fig. 3(b), diagonal coupling reduces equally ρ_{m-n} for all nonzero even $m-n$. This is clearly reflected in the sizes of L_ρ for the three cases displayed in Fig. 3(b): 5.95 ($T_R = 0, \phi = 1, J_R = g = 0$), 2.93 ($T_R = 0.2, \phi = 1, J_R = g = 0$) and 3.71 ($T_R = 0, g = \phi = 1, J_R = 0$). With increasing temperature, ρ_{m-n} for $m-n = \pm 4, \pm 6, \pm 8$ vanishes much faster than $m-n = \pm 2$. For diagonal coupling only, ρ_{m-n} is completely localized on $m-n=0$. Off-diagonal coupling thus induces localization as well as assists transport of electronic excitations.

Addition of the transfer integral J destroys the folded polaron band structure by lowering the zone center energy $E_{K=0}$ [cf. Fig. 4(b)]. Consequently, the structure of ρ_{m-n} is expanded while retaining the oscillatory feature in Fig. 3(b). As the zone center energy $E_{K=0}$ is lowered to the level of $E_{K=\pm\pi/2}$, the polaron band has a rather flat structure at the zone center, as illustrated in Fig. 4(c) for the case of $\phi = 1, J_R = 2$, causing the reduced density matrix to change abruptly as the temperature is raised from zero. In Fig. 3(c) we compare ρ_{m-n} for two low temperatures $T_R = 10^{-3}$ and 10^{-2} for $J_R = 8, \phi = 1$. A temperature increase of one hundredth of the phonon frequency drastically affects the profile of ρ_{m-n} due to a flat band bottom at the zone center, and L_ρ also drops from 13.9 ($T_R = 10^{-3}$) to 8.94 ($T_R = 10^{-2}$). For sufficiently large transfer integrals, the polaron band acquires a similar shape as the weak coupling band of diagonal exciton-phonon-coupling, and so does the reduced density matrix ρ_{mn} .

So far our calculations were based on the assumption that the temperature is much lower than the phonon frequency $T_R \ll 1$, which is typically the case for optical phonons even at room temperature. Aggregates may have strong coupling to low-frequency solvent modes. Nuclear spectral densities representing coupling to low-frequency modes have been used to fit photon-echo measurements in light-harvesting complexes.¹⁴ This corresponds to the opposite limit $T_R \equiv T/\omega_0 \gg 1$ (here ω_0 denotes a typical frequency of low-energy solvent modes) and the adiabatic polaron theory can be applied. The calculation of the polaron wave functions is greatly simplified when nuclear motions are much slower than the electronic ones. In this case we can adopt the Born-Oppenheimer (adiabatic) approximation. The adiabatic polaron theory was first developed by Pekar⁵¹ for an analogous continuum Hamiltonian—the Fröhlich Hamiltonian—describing a slow electron moving in an ionic crystal.⁵² Later the Pekar-type adiabatic solution was generalized to the Holstein Hamiltonian for molecular crystals.^{33,34} Both the large and small adiabatic polaron can be captured

by the Holstein Hamiltonian, while in the Fröhlich Hamiltonian only the large polaron is physically meaningful. If the characteristic phonon frequency is small compared to the splitting between exciton levels the lattice kinetic energy can be neglected in the zero-order adiabatic approximation.⁵³

For the diagonal coupling we get (see Appendix E for the derivation)

$$\rho_{mn} = \frac{1}{L_0} \sum_s \Psi^*(m+s) \Psi(n+s), \quad (48)$$

where the exciton wave function satisfies the discrete nonlinear Schrödinger equation^{33,34,54}

$$-J[\Psi(n+1) + \Psi(n-1)] - 4\lambda |\Psi(n)|^2 \Psi(n) = E\Psi(n), \quad (49)$$

where 2λ is the Stokes shift of a single molecule ($2\lambda = g^2\omega_0$ for the Holstein model) and E is the polaron energy. For large polarons (i.e., when the polaron size l_p is much larger than the lattice constant but still smaller than the system's size), one can apply the one-dimensional infinite-size continuum model, which yields the following (soliton) solution of Eq. (49).^{33,34}

$$\Psi(n) = \sqrt{\frac{1}{2a_0}} \operatorname{sech}\left(\frac{n}{a_0}\right), \quad (50)$$

with $a_0 \equiv J/\lambda$. Solutions of the continuum version of Eq. (49) on a ring, which generalize Eq. (50) to finite systems have been obtained recently in Ref. 55. The connection between the soliton solutions and the Toyozawa Ansatz is discussed in Appendix D. In Fig. 3(d), we show the reduced density matrices calculated using Eqs. (48) and (50). For the three strengths of nonlinearity shown $a_0 = 3, 4, 5$, the corresponding values of L_ρ are 17.9, 17.7 and 16.8, respectively.

Equation (48) allows us to treat effects of disorder and phonon coupling on exciton coherence size in the same fashion. In the case of static disorder $\Psi(m)$ is a localized exciton wave function, whereas in the polaron picture represented by the Toyozawa Ansatz, $\Psi(m)$ is the self-trapped exciton wave function represented by ψ_m^K in Eq. (41). In the case of static disorder, Eq. (48) should be averaged over disorder realizations with the canonical distribution [see Eq. (30)]. For strong or intermediate exciton-phonon-coupling the averaging of Eq. (48) is given by Eq. (43) by setting $\langle \Lambda_{n'}^K | \Lambda_n^K \rangle = \delta_{n'n}$. In the adiabatic polaron approach $\Psi(m)$ is the solution of Eq. (49).

V. SUPERRADIANCE IN CYCLIC AGGREGATES

It was shown in Sec. II that the superradiance enhancement factor depends on two ingredients: the exciton density matrix and the window function M_{ij} which carries information regarding the aggregate geometry. In this section we consider various models for dipole orientations and combine them with the calculation of the density matrix presented in the last two sections to explore the superradiant behavior of the LH2 complexes.

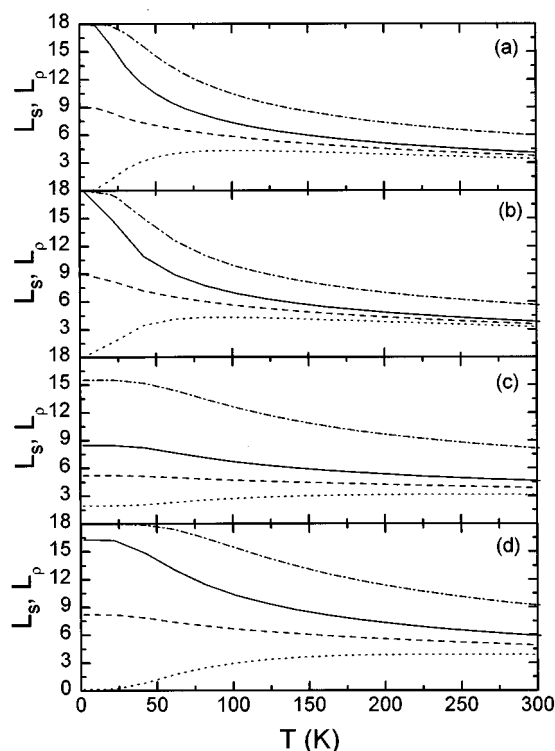


FIG. 5. Variation of L_s with temperature. Solid: model III; dashed: model II; dotted: model I; dashed-dotted: L_ρ . (a) Without disorder and exciton-phonon-coupling. (b) Diagonal coupling, the weak coupling limit $\kappa \rightarrow 0$ and $J_R = 0.8$. (c) Diagonal coupling, $J_R = 8$, $\kappa = 0.5$. $\omega_0 = 1253 \text{ cm}^{-1}$. (d) Off-diagonal coupling, $\phi = 1$ and $J_R = 5$. $\omega_0 = 1253 \text{ cm}^{-1}$.

The window function for a cyclic aggregate can be readily calculated. Denoting the angle between the molecular dipole and the aggregate plane by Θ we obtain:

$$M_{mn} = d^2 \left[\sin^2 \Theta + \cos^2 \Theta \cos \left(\frac{2\pi(m-n)}{L_0} \right) \right]. \quad (51)$$

It follows from the circular symmetry, that ρ and M are diagonal in the same basis set and the superradiant states are

$$\phi_{1,2}(m) = \frac{1}{\sqrt{L_0}} e^{\pm i2\pi m/L_0}, \quad \phi_3(m) = \frac{1}{\sqrt{L_0}}, \quad (52)$$

with the corresponding oscillator strengths

$$\bar{f}_1 = \bar{f}_2 = \frac{1}{2} d^2 L_0 \cos^2 \Theta, \quad \bar{f}_3 = d^2 L_0 \sin^2 \Theta. \quad (53)$$

The state ϕ_3 has a transition dipole orthogonal to the aggregate's plane, whereas ϕ_1 and ϕ_2 have an in-plane dipole. Combining Eqs. (15) and (51)–(53) we have for the superradiance factor:

$$L_s = \left(\cos^2 \Theta \frac{\rho_1 + \rho_2}{2} + \sin^2 \Theta \rho_3 \right) L_0, \quad (54)$$

with $\rho_1 + \rho_2 + \rho_3 \leq 1$.

We first examine the effect of finite temperature. Figure 5(a) shows the variation of L_s with temperature for three orientations of the dipoles with respect to the ring: model I ($\Theta = 0^\circ$), model II ($\Theta = 45^\circ$), and model III ($\Theta = 90^\circ$). L_ρ

displayed for comparison decreases with increasing temperature [see Fig. 1(a)]. For model III the temperature dependence of L_s is close to that of L_ρ : both decrease from 18 for low temperatures to 1 in the high temperature limit. However, for model I, L_s shows a very different temperature dependence: at low temperatures the density matrix is completely delocalized, and the summation over all the inner products of the dipole vectors in the calculation of L_s yields $L_s = 0$. With increasing temperature the coherence size L_ρ decreases and L_s becomes finite and eventually reaches a maximum when L_ρ is somewhat larger than half the system size. At high temperatures, all three models have similar superradiance factors which eventually approach 1. It follows from Eq. (54) that the superradiance factor for model II is simply the average of models I and III. It is therefore easy to calculate L_s for all angles Θ , using the curves for models I and III.

Figures 5(b)–5(d) display the temperature-dependence of L_s and L_ρ due to diagonal and off-diagonal exciton-phonon-coupling. Within the polaron model as outlined Sec. IV, localization of $\rho_{mm'}$ may have several origins. Increased temperature results in smaller L_ρ . This is clearly shown when the bandwidth $4J$ is less than the Einstein phonon frequency ω_0 ($J_R < 1$) so that the bare exciton band does not cross into the one-phonon scattering continuum. For $J_R > 1$, the weak coupling limit is nonperturbative in the sense that the $\kappa \rightarrow 0^+$ polaron band is different from the bare exciton band due to level repulsion from the phonon continuum.^{56–59}

In Fig. 5(b), we display L_ρ and the superradiance length L_s for our three models and for $J_R = 0.8$ in the weak coupling limit ($\kappa \rightarrow 0$). At zero temperature, both L_ρ and the superradiance length L_s for parallel dipoles (model III) are equal to the size of the system, 18. Due to the momentum selection rule, L_s for the in-plane dipole configuration (model I) reaches a maximum at a temperature whereby the $K = 2\pi/18$ state is most populated. L_ρ and the superradiance length L_s for $\Theta = 0^\circ, 45^\circ, 90^\circ$ are shown in Fig. 5(c) for intermediate exciton-phonon coupling $\kappa = 0.5$, $J_R = 8$. At zero temperature the superradiance length L_s for parallel dipoles is only half the size of the ring, and L_ρ is also less than 18. For strong exciton-phonon coupling, the superradiance size L_s is independent of temperature. In Fig. 5(d) we show L_ρ and the superradiance length L_s for models I, II and III as a function of the temperature for $J_R = 4$, $\phi = 1$ and $g = 0$. The dependence of the superradiance length L_s on temperature is very similar to the diagonal coupling case.

In Fig. 6(a) we display L_s and L_ρ versus the static disorder parameter σ at 4 K. The curves are slightly different, but their general appearance and limits are similar to Fig. 5(a). Figure 6(b) repeats the calculations of Fig. 6(a) for a higher temperature (100 K). Due to the temperature-induced loss of coherence, L_ρ and L_s for model III are smaller than the system size for weak disorder, and L_s for model I no longer vanishes. Analogous to Fig. 6(a), with increasing disorder L_s becomes similar for all models. For very strong disorder, L_ρ as well as L_s approach 1.

The correlations between L_s and L_ρ are clearly shown in Fig. 7(a), where we display them for the different localiza-

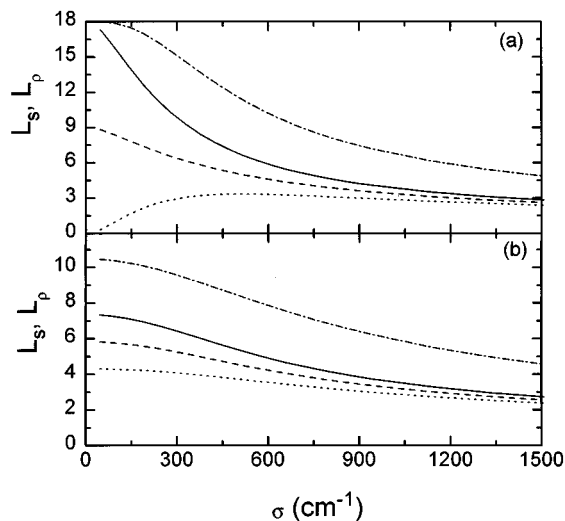


FIG. 6. Variation L_s with disorder strength, in the absence of exciton-phonon coupling. (a) $T=4$ K and (b) $T=100$ K. Solid: model III; dashed: model II; dotted: model I; dashed-dotted: L_ρ .

tion mechanisms and dipole orientations. For the two localization mechanisms considered in Fig. 7(a) (temperature- and disorder-induced dephasing) we find a very similar correlation between L_s and L_ρ in models I and III, which demonstrates that the superradiance enhancement factor is in both cases primarily determined by the off-diagonal spread of the density matrix L_ρ , and that both mechanisms influence the superradiative enhancement factor in a similar fashion. In Fig. 7(b), L_s from model III is plotted vs L_ρ within the polaron approach for different temperatures, intermolecular couplings and diagonal exciton-phonon couplings. This again shows the strong correlation between L_s and L_ρ is not sensitive to the underlying mechanisms.

We have identified the density matrix size L_ρ as the primary factor in determining the superradiance size L_s . This allows us to predict L_s using L_ρ , regardless of the specific microscopic mechanism that determines L_ρ . A commonly used measure of the exciton localization length is provided by the inverse participation ratio of a wave function $\Psi_\alpha(m)$ ³⁶

$$l_\alpha \equiv \frac{1}{\sum_m |\Psi_\alpha(m)|^4}. \quad (55)$$

The thermally averaged size associated with the wave function is defined by:

$$l_\psi \equiv Z^{-1} \sum_\alpha l_\alpha \exp(-\epsilon_\alpha/T). \quad (56)$$

We shall now discuss the connection between l_ψ and L_ρ . At low temperatures L_ρ depends on exciton localization and is related to l_ψ . The numerical factor which relates the two depends on the form of the wave function and the system size L_0 . To illustrate this point we plot in Fig. 8(a) the dependence of L_ρ on l_ψ for different models. Assuming a uniform wave function $\Psi(m) = \theta(m) \theta(l_\psi - m) / \sqrt{l_\psi}$ where $\theta(m)$ is the Heaviside function, we obtain

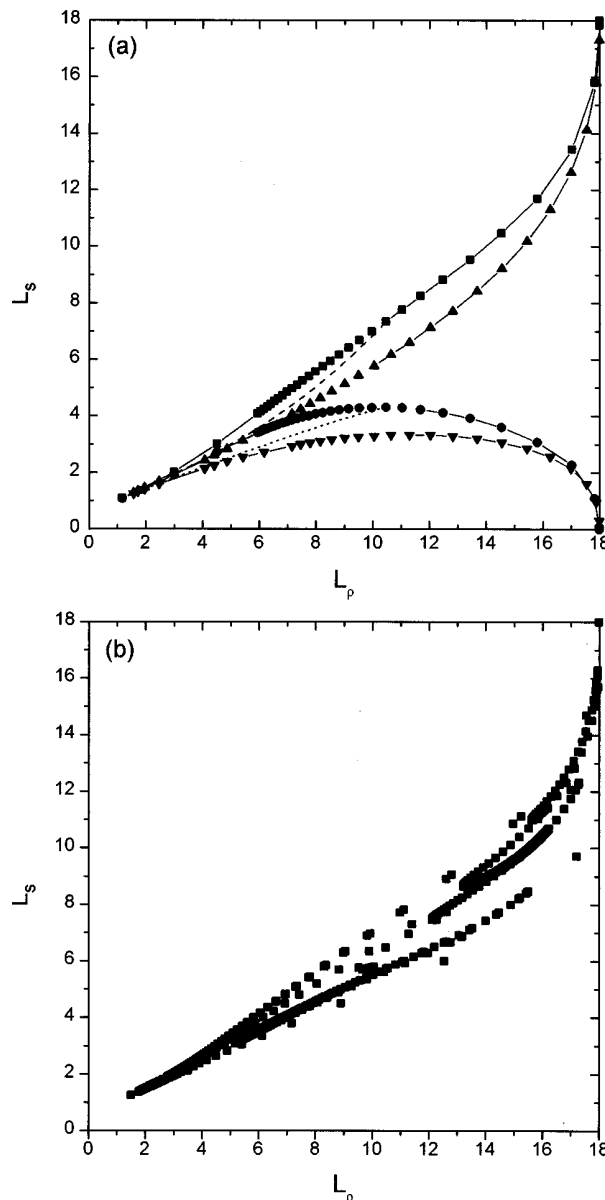


FIG. 7. Correlation between the superradiance enhancement factor L_s and the density matrix size L_ρ . (a) Squares: model III for different temperatures, triangles up: model III for different disorder strengths at $T=4$ K; dashed line: model III for different disorder strengths at $T=100$ K, circles: model I for different temperatures; triangles down: model I for different disorder strengths at $T=4$ K; dotted line: model I for different disorder strengths at $T=100$ K; (b) model III for different temperatures T , intermolecular couplings J and diagonal exciton-phonon coupling strength g .

$$L_\rho = \frac{3l_\psi^3}{2l_\psi^2 + 1}, \quad \text{for } l_\psi \leq \frac{L_0}{2}; \quad (57)$$

$$L_\rho = \frac{3l_\psi^4}{l_\psi(2l_\psi^2 + 1) + (2l_\psi - L_0)^3 - (2l_\psi - L_0)}, \quad \text{for } l_\psi > \frac{L_0}{2}.$$

In particular $L_\rho = l_\psi$ when $l_\psi = L_0$. Therefore in the absence of disorder and at low temperatures ($T=4$ K) both measures give $L_\rho = l_\psi = L_0 = 18$, since the lowest exciton is completely delocalized. With increasing disorder however, they start to

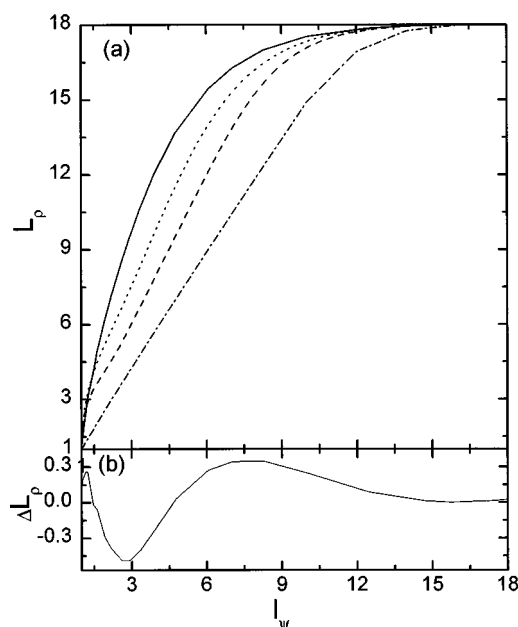


FIG. 8. (a) L_ρ versus l_ψ of the lowest exciton wave function for different models. Dashed-dotted: uniform wave function; dashed: Gaussian wave function; dotted: sech wave function [Eq. (50)]; solid: $T=4$ K with varying disorder. (b) Difference between the solid curve of (a) and the Padé approximant Eq. (58).

differ, since the exciton wave function is no longer uniform. For $L_0 \gg l_\psi \gg 1$, we have $L_\rho \approx 1.5l_\psi$ as shown in Fig. 8(a). For the Gaussian wave function $\Psi(m)$, we have $L_\rho = 2l_\psi$ if $L_0 \gg l_\psi \gg 1$. The soliton wave functions Eq. (50) show a similar behavior. Monte Carlo averaging over diagonal disorders yields the solid curve in Fig. 8(a). An excellent fit is obtained using the Padé approximant [see Fig. 8(b)]

$$L_\rho = \frac{1 + 7.88(l_\psi - 1)}{1 + 0.316(l_\psi - 1) + 0.00393(l_\psi - 1)^2}. \quad (58)$$

These examples illustrate that the coherence length L_ρ representing the number of coherently coupled molecules is closely related to the size of the corresponding wave functions which is usually defined through the inverse participation ratio l given by Eq. (55) where $l = l_\psi$ for the model of static disorder and $l = l_p$ for the case of exciton-phonon coupling. However, the relations between these quantities contain important numerical factors representing the wave function shape⁶⁰ and the system size. All models show a very similar behavior with the numerical ratio of l_ψ and L_ρ varying from 1.0 to 3.3 depending on the model and the value of l_ψ . This has a very important implication for analyzing experimental data on the superradiance enhancement factor L_s in light-harvesting complexes.²²

In all four cases shown in Fig. 8(a), the wave functions are nonoscillatory and l_ψ is the only factor which determines L_ρ . This situation is changed as the temperature is increased. It follows from Eq. (30) that both the amplitude and the phase of thermally populated exciton wave functions affect L_ρ . At low temperatures only excitons at the bottom of the band with nonoscillatory wave functions are populated.

Therefore L_ρ is determined by localization of the amplitude and is related to l_ψ . In the absence of disorder exciton states are delocalized over the entire aggregate and L_ρ is determined by oscillations of wave functions corresponding to higher-energy excitons which are populated when the temperature is raised. This implies that the characteristic length l_T reflects the phase oscillations of the exciton wave functions. In a disordered aggregate at low temperatures when $l_\psi \ll l_T$, phase oscillations are negligible and L_ρ is related to l_ψ . As the temperature is raised and higher-energy excitons become populated, l_ψ increases since localization is weaker at higher energies whereas phase oscillations become more important, as reflected in the decrease of l_T . L_ρ then decreases while l_ψ increases. In this intermediate region $l_\psi \sim l_T$, L_ρ is influenced by the competition of the amplitude and the phase-induced mechanisms. At higher temperatures $l_T \ll l_\psi$, exciton localization becomes irrelevant and L_ρ is determined by the thermal size l_T . This can be illustrated as follows: our numerical simulations of the thermal- and disorder-averaged density matrix $\langle \rho \rangle$, with $\sigma = 377 \text{ cm}^{-1}$ gives $L_\rho = 13.7$. Using Eq. (56) we then obtain $l_\psi = 4.8$, so that $L_\rho/l_\psi \approx 3$. We recall that for these parameters we find a superradiance enhancement factor of $L_s = 3.2$ for model I. With increasing disorder both measures become more localized. For $\sigma = 754 \text{ cm}^{-1}$ and $T = 4 \text{ K}$ we obtain $L_\rho = 8.6$ and $l_\psi = 2.6$, and their ratio is 3.3. With increasing temperature, due to the contribution of energetically higher exciton states which are more delocalized, l_ψ increases, while L_ρ decreases. For $T = 300 \text{ K}$ we have $L_\rho = 5.8$ and $l_\psi = 6.6$. These examples illustrate an interplay of the characteristic sizes l_ψ and l_T in determining the coherence size L_ρ . We reiterate that superradiance is strongly affected by geometry and L_s is not necessarily proportional to l_ψ , i.e., for weak disorder L_s is determined by the loss of coherence $L_0 - L_\rho$ rather than l_ψ . Usually one can divide the aggregate into domains L_g (g stands for geometry) within which molecular dipoles are oriented in more or less the same direction. These directions are different for different domains and the total dipole of the aggregate vanishes due to cancellation of contributions from different domains. At long times, when excitons are equilibrated, L_ρ is independent on the system's geometry. In contrast, the size L_g depends only on the dipole orientations (and the system's symmetry) and is independent on the state of the aggregate. It is easy to see that for a given geometry (and L_g) there is an optimal value of the coherence size L_ρ , which maximizes the superradiance, namely $L_\rho \approx L_g$.

The dipole orientations in LH1 and LH2 imply that the fluorescence should vanish if all monomers emit coherently (i.e., $L_\rho = L_0$).⁶¹ The factor L_s can then be small in two cases: either $L_\rho \ll L_0$ where we have $L_s \approx L_\rho$ (since the dipoles emitting coherently are almost parallel) or $L_0 - L_\rho \ll L_0$ where we have $L_s \approx L_0 - L_\rho$ and the signal is proportional to the measure of coherence destruction. This means that L_s is not necessarily proportional to l_ψ . For example, in calculations performed for LH2⁶¹ $l_\psi \approx 6$, $L_\rho \approx 15$ and $L_s \approx 3$ which satisfies $L_s \approx L_0 - L_\rho$. This could explain the difference between low-temperature superradiance of LH1 ($L_s \approx 9$) and LH2 ($L_s \approx 3$) observed in Ref. 22 despite close values of

parameters for both complexes. The differences in L_s could be attributed to different geometric factors (and window functions) resulting from the different number of pigments ($L_0 = 32$ versus $L_0 = 18$) in these complexes.

VI. DISCUSSION

Spectroscopic properties of J-aggregates^{24,25,27,62,63} and light-harvesting complexes^{3,4,9,14,22,64} are often related to a coherence size known as the exciton delocalization length [cf. Eq. (56)]. In the absence of disorder and exciton-phonon interaction, the exciton states are delocalized over the entire aggregate, and the exciton delocalization length is equal to the aggregate size. Since in infinite one-dimensional disordered systems all exciton states become localized,³¹ static disorder induces a finite (Anderson-type) exciton delocalization length. Effects of exciton localization on optical signals of disordered aggregates can be rationalized by examining properties of individual states and their contributions to l_ψ .

Effects of nuclear motions on the exciton localization length have been denoted dynamical localization.^{14,62} Dynamical localization is much more complex than its static counterpart, since excitons are coupled to a large (often macroscopic) number of nuclear degrees of freedom. The only practical way to introduce an exciton delocalization length in this case is through observables which involve exciton variables. Such observables can always be represented in terms of Green functions of exciton operators^{36,49,65} and in some cases in terms of reduced exciton density matrices (which constitute a particular case of Green functions). Despite this formal difficulty which can be overcome by applying the Green function formalism, it is clear that there is a substantial physical difference between static and dynamical localization: in aggregates with exciton-phonon coupling but without static disorder excitons are self-trapped^{33,34} rather than localized. This implies that a natural measure for the exciton dynamical delocalization will be the polaron size l_p defined in Sec. IV as the size of the self-trapped exciton wave function Ψ_{m-n}^K which enters the expression for the polaron wave function [Eq. (41)]. The main difference between static localization and dynamic (self-trapping) localization is that a localized exciton is confined in a certain region in space whereas the exciton density in the polaron wave function is spread over the entire aggregate. However, since the wave function of the self-trapped exciton ψ_{m-n}^K is localized, self-trapping and localization have common features and similar effects on some spectroscopic measurements.

In the remainder of this section we discuss how static and dynamical localization show up in various spectroscopic techniques. Exciton localization naturally leads to a decrease of the superradiance factor in the time-resolved emission^{20,22,24,61} and affects energy transfer which affects in depolarization measurements.^{3,4,64} In particular, in the absence of nuclear motions no transport should take place in a system with localized excitons, and the fluorescence will retain its initial polarization at all times. In the presence of nuclear

motions exciton localization affects transport properties by increasing the depolarization timescale.

Static localization of excitons also affects the temperature dependence of fluorescence decay^{24,63} and pump-probe signals^{9,25,27,61,62} in a more delicate way. The effect may be rationalized using the Mott picture of Anderson localization which implies that localized states with close energies must be spatially separated.⁶⁶ This leads to a qualitative picture whereby the aggregate can be divided into noninteracting segments whose sizes are equal to the localization length. The signals from a large disordered aggregate can therefore be related to the signal from a homogeneous aggregate whose physical size is given by the localization length.

It has been shown in Ref. 61 that polaron formation (self-trapping) and static localization lead to similar features in the pump-probe signal for long time delays. In both cases the shift between positive (induced-absorption) and negative (bleaching) peaks in the differential absorption reflects the energy difference between the lowest and the next lowest excitons. This is in turn related to the polaron binding energy E_p (i.e., the binding energy of the self-trapped exciton) in the dynamical case, and is given by the minimal energy splitting between exciton states located in the same region in space.⁶⁷ For weak exciton-phonon coupling⁶¹ the pump-probe signal was related to the one-exciton Green function, and the shift in the pump-probe signal was related to the exciton mean-free path which plays the role of the coherence size for the pump-probe signal.

The exciton delocalization length can show up directly in transport processes. Although aggregate sizes are usually smaller than the optical wavelength, nonuniform population distributions are obtained by optical excitation of light-harvesting complexes with polarized light due to dipole orientations. Population relaxation can be observed by depolarization measurements.^{3,4} A model in which an excitation is localized on a dimer due to static disorder has been used^{3,4} to fit energy transfer experiments. The possibility of dynamical contributions to exciton localization in the context of transport phenomena has been discussed.¹⁴ A theory of energy transfer in molecular aggregates with strong exciton-phonon coupling using canonical transformations in the joint exciton-phonon space has been developed.^{45,68} The role of polaron effects on the energy transfer has been discussed for the cases of small and large polarons.^{45,69} An application of transport theories will be to connect the exciton delocalization size due to coupling to nuclear motions with the depolarization timescale observed in Refs. 3 and 4. An interesting attempt to introduce a coherence size related to transport by means of the Green function techniques in Ref. 64 for a system with static disorder and exciton-phonon coupling has been treated within the Redfield theory^{44,70} with the Redfield relaxation operator taken in the Haken-Strobl form.^{71,72} However, the Green function $G_{ii,ii}^{(0)}$ used in Eq. (39) of Ref. 64 to define the participation ratio is related to a model with a finite lifetime rather than homogeneous dephasing, for which most calculations have been made. This can be clearly seen from Eq. (40) of Ref. 64 which shows the same rate Γ for the decay of populations and coherences. Thus the coher-

ence size defined in Ref. 64 is related to exciton lifetime and not to pure dephasing processes due to exciton-phonon coupling.

In this paper, utilizing the DW representation we have related the time-resolved fluorescence signal to the reduced exciton density matrix. Superradiance is usually attributed to coherent emission of a set of electronic dipoles confined within a region of a size much smaller than the wavelength of the emitted light. This coherence can be partially or completely eroded by interactions with additional degrees of freedom such as nuclear motions and static disorder. The density matrix further allows us to visualize various mechanisms by staying in the exciton phase space (as opposed to the joint exciton-phonon space). This is impossible using a wave function description. The calculations presented here clearly show that the coherence size of the density matrix is the natural lengthscale which controls cooperativity in spontaneous emission. Calculations based on eigenstates are numerically expensive and often do not lead to a clear insight. Since properties of individual eigenstates are usually highly averaged and lost in observables. For example, the thermal density matrix at high temperatures is localized, although the individual exciton states are fully delocalized! The destruction of superradiance is determined by the density matrix. It is hard to envision this effect in a unified fashion for various models by examining individual eigenstates. Our calculations demonstrate that the exciton localization length l_ψ due to static disorder and the size of self-trapped exciton l_p in the case of strong exciton-phonon-coupling have similar signatures in the reduced exciton density matrix and superradiance.

ACKNOWLEDGMENTS

We wish to thank R. van Grondelle, A. A. Muentner and E. I. Rashba for useful discussions. The support of the Air Force office of scientific research, the National Science Foundation Center for Photoinduced Charge Transfer, and the National Science Foundation through Grants No. CHE-9526125 and No. PHY94-15583 is gratefully acknowledged.

APPENDIX A: THE SUPERRADIANT STATES

In this Appendix we prove the statements in Sec. III made with regard to the eigenstates of the window function M . To that end we define a linear map $\mathbf{D}: V \rightarrow \mathcal{R}^3$ from the L_0 dimensional space of real one-exciton functions to the space of real 3-dimensional vectors by

$$\mathbf{D}\phi = \sum_m \mathbf{d}_m \phi(m). \quad (\text{A1})$$

The matrix M viewed as a bilinear form of V can be written in a form:

$$M(\phi, \Psi) = \mathbf{D}(\phi) \cdot \mathbf{D}(\Psi). \quad (\text{A2})$$

Since \mathcal{R}^3 is 3-dimensional and V is L_0 -dimensional there is a $(L_0 - 3)$ dimensional subspace $V_1 \subset V$ with $\mathbf{D}(V_1) = 0$. Let V_0 be the 3-dimensional orthogonal component to V_1 , then $M(\phi, \Psi) \neq 0$ only if both $\phi, \Psi \in V_0$, which means that M

can be viewed as a bilinear form on V_0 and all eigenstates of M viewed as a linear operator $M: V \rightarrow V$ with nonzero eigenvalues belong to V_0 . M can be diagonalized on V_0 in an orthogonal basis set represented by ϕ_α , $\alpha = 1, 2, 3$. We then denote for $\alpha = 1, 2, 3$

$$\mathbf{d}_\alpha = \sum_m \mathbf{d}_m \phi_\alpha(m). \quad (\text{A3})$$

In the notation of Sec. II, ϕ_α are the superradiant states with transition dipoles \mathbf{d}_α . The relations $\mathbf{d}_\alpha \cdot \mathbf{d}_\beta = 0$ for $\alpha \neq \beta$ and $f_\alpha = |\mathbf{d}_\alpha|^2$ follows from the fact that M is diagonal in the basis set of superradiant states and using Eqs. (A1) and (A2).

APPENDIX B: WINDOW FUNCTION FOR DIMERIZED CIRCULAR AGGREGATES

In this Appendix we present expressions for the window functions for a circular aggregate with two molecules in a unit cell. Let Θ_j , $j = 0, 1$ be the angles which molecular dipoles in a unit cell form with the aggregate plane and ϕ_j are the angles between their projections into the plane and the circle. A simple calculation yields:

$$\begin{aligned} M_{2m+j, 2n+k} &= d^2 \left\{ \sin \Theta_j \sin \Theta_k + \cos \Theta_j \cos \Theta_k \right. \\ &\quad \left. \times \cos \left[\frac{2\pi}{L_0} (2m - 2n + j - k + \phi_j - \phi_k) \right] \right\}, \quad (\text{B1}) \end{aligned}$$

with $m, n = 0, 1, \dots, (L_0 - 2)/2$ and $j, k = 0, 1$.

The superradiant states can be evaluated using the approach of Appendix A and have the following form:

$$\begin{aligned} \Phi_3(2m+j) &= \left[\frac{L_0}{2} (\sin^2 \Theta_0 + \sin^2 \Theta_1) \right]^{-1/2} \sin \Theta_j, \\ \Phi_{1,2}(2m+j) &= \left[\frac{L_0}{2} (\cos^2 \Theta_0 + \cos^2 \Theta_1) \right]^{-1/2} \\ &\quad \times \cos \Theta_j \exp \left\{ \pm i \left[\frac{2\pi}{L_0} (2m+j) + \phi_j \right] \right\}, \quad (\text{B2}) \end{aligned}$$

with the corresponding oscillator-strengths

$$\begin{aligned} \bar{f}_3 &= d^2 \frac{L_0}{2} (\sin^2 \Theta_0 + \sin^2 \Theta_1), \\ \bar{f}_1 = \bar{f}_2 &= d^2 \frac{L_0}{4} (\cos^2 \Theta_0 + \cos^2 \Theta_1). \quad (\text{B3}) \end{aligned}$$

APPENDIX C: DENSITY MATRIX OF EXCITONS COUPLED TO PHONONS

In this Appendix we discuss perturbative treatments of exciton-phonon coupling on the reduced exciton density matrix. For weak exciton-phonon-coupling the reduced exciton density matrix adopts the Boltzmann form in the exciton basis set [cf. Eqs. (29) and (30)] at long time. This is no longer the case as the exciton-phonon coupling is increased. This can be shown using perturbative arguments. We con-

sider the generalized master equation (GME) for the evolution of the reduced exciton density matrix ρ_{mn} which can be derived using the projection operator techniques.^{38,43} The kernel of the GME can be explicitly calculated perturbatively in the exciton-phonon-coupling. The long-time value of ρ_{mn} is then the stationary point of the GME

$$-i[h, \rho]_{mn} - \sum_{kl} R_{mn,kl} \rho_{kl} = 0, \quad (C1)$$

where the matrix $h_{ij} = \Omega_i \delta_{ij} + J_{ij}(1 - \delta_{ij})$ represents one-exciton Hamiltonian and $R_{mn,kl}$ is the Redfield tensor,^{44,70} given by the zero-frequency value of the GME kernel. When the Redfield tensor is calculated to lowest (second) order in exciton-phonon coupling, Eq. (C1) yields the Boltzmann distribution of bare excitons⁷⁰ given by Eqs. (29) and (30) for ρ_{mn} . Finding ρ_{mn} from Eq. (C1) with the Redfield tensor $R_{mn,kl}$ calculated in the next (fourth) order in coupling strength will show a deviation of ρ_{mn} from the Boltzmann distribution.

Another perturbative argument can be made as follows: assuming that at long times the full density matrix ρ_M of the joint exciton-phonon system adopts the canonical form, the reduced exciton density matrix ρ_{mn} can be represented as

$$\rho_{mn} = \text{Tr}(B_m^\dagger B_n \rho_M). \quad (C2)$$

The r.h.s. of Eq. (C2) can be evaluated perturbatively in the exciton-phonon coupling strength, e.g., by applying the Matsubara Green's function techniques.⁶⁵ The zero-order result yields Eq. (30) whereas the second-order contribution results in deviations of ρ_{mn} from the bare Boltzmann distribution. Deviation from the Boltzmann distribution of bare exciton at long times for weak exciton-phonon-coupling has been demonstrated in Ref. 23. However, the non-Boltzmann asymptotic behavior of the exciton distribution originates from neglecting environmental (e.g., solvent) nuclear modes in the model: The system does not have enough phonons to equilibrate. Adding solvent modes with a continuous spectrum to that model will lead to a Boltzmann distribution of bare excitons at long times within the formalism of Ref. 23, which is based on perturbative in exciton-phonon coupling calculation of the GME^{43,73} with memory. This implies that the results of Ref. 23 describe a situation with weak coupling to solvent modes for intermediate timescales when coupling to solvent modes is unimportant and exciton dephasing is induced by the aggregate intermolecular and intramolecular modes.

APPENDIX D: TOYOZAWA'S ANSATZ FOR THE POLARON WAVE FUNCTION

In this Appendix we present the details of the Toyozawa Ansatz for polaron wave functions. We start with generalizing the Holstein Hamiltonian, also known as the molecular crystal model, by adding the linear off-diagonal exciton-phonon coupling:

$$\hat{H} = \hat{H}^{ex} + \hat{H}^{ph} + \hat{H}^{ex-ph}, \quad (D1)$$

$$\hat{H}^{ex} = -J \sum_n B_n^\dagger (B_{n+1} + B_{n-1}), \quad (D2)$$

$$\hat{H}^{ph} = \hbar \omega_0 \sum_n b_n^\dagger b_n, \quad (D3)$$

$$\begin{aligned} \hat{H}^{ex-ph} = & g \hbar \omega_0 \sum_n B_n^\dagger B_n (b_n^\dagger + b_n) \\ & + \frac{\phi}{2} \hbar \omega_0 \sum_{nl} [B_n^\dagger B_{n+1} (b_l^\dagger + b_l) (\delta_{n+1,l} - \delta_{nl}) \\ & + B_n^\dagger B_{n-1} (b_l^\dagger + b_l) (\delta_{nl} - \delta_{n-1,l})]. \end{aligned} \quad (D4)$$

Here $|0\rangle$ is the vacuum state for both the exciton and the phonon degrees of freedom, and B_n^\dagger (b_n^\dagger) creates an exciton (phonon) on site n . ω_0 is the Einstein phonon frequency, J is the exciton transfer integral between nearest-neighbor sites, and g (ϕ) is the diagonal (off-diagonal) exciton-phonon coupling strength. The original Holstein model contains only diagonal exciton-phonon-coupling. The Hamiltonian Eq. (D1) can be obtained from Eq. (1) by expanding molecular frequencies $\Omega_n(\mathbf{q})$ and intermolecular couplings $J_{mn}(\mathbf{q})$ up to first order in nuclear coordinates \mathbf{q} . We also assume the nearest neighbor form of intermolecular couplings $J_{mn}(\mathbf{q})$ and Einstein phonons.

Following Toyozawa,⁵⁰ we construct the one-exciton wave function

$$\begin{aligned} |K\rangle = & \sum_n e^{iKn} \sum_{n_1} \psi_{n_1-n}^K B_{n_1}^\dagger \exp \left[- \sum_{n_2} (\lambda_{n_2-n}^K b_{n_2}^\dagger \right. \\ & \left. - \lambda_{n_2-n}^{K*} b_{n_2}) \right] |0\rangle. \end{aligned} \quad (D5)$$

The variationally optimized parameters λ_n^K describe the phonon distortion of site n , and ψ_n^K are the corresponding exciton amplitudes. Equation (D5) is equivalent to Eq. (41) where the phonon wave functions $|\Lambda_n^K\rangle$ are explicitly written in terms of phonon coherent states

$$|\Lambda_n^K\rangle = \exp \left[- \sum_{n_2} (\lambda_{n_2-n}^K b_{n_2}^\dagger - \lambda_{n_2-n}^{K*} b_{n_2}) \right] |0\rangle_{ph}. \quad (D6)$$

Equation (D5) can be alternatively represented in momentum-space as

$$\begin{aligned} |K\rangle = & L_0^{-1/2} \sum_{nk} e^{i(K-k)n} \psi_k^K B_k^\dagger \\ & \times \exp \left[- L_0^{-1/2} \sum_q (\lambda_q^K e^{-iqn} b_q^\dagger - \lambda_q^{K*} e^{iqn} b_q) \right] |0\rangle, \end{aligned} \quad (D7)$$

where B_k^\dagger , b_q^\dagger , ψ_k^K and λ_q^K are Fourier transforms of B_n^\dagger , b_n^\dagger , ψ_n^K and λ_n^K :

$$B_k^\dagger = L_0^{-1/2} \sum_n e^{-ikn} B_n^\dagger, \quad (D8)$$

$$b_q^\dagger = L_0^{-1/2} \sum_n e^{-iqn} b_n^\dagger, \quad (\text{D9})$$

$$\psi_k^K = \sum_n e^{ikn} \psi_n^K, \quad (\text{D10})$$

$$\lambda_q^K = \sum_n e^{iqn} \lambda_n^K. \quad (\text{D11})$$

The exciton amplitudes ψ_n^K serve as weights in a linear superposition of phonon coherent states if Toyozawa's Ansatz (D5) is viewed in a different form:⁷⁴

$$|K\rangle = L_0^{-1/2} \sum_n e^{iKn} B_n^\dagger \sum_{n_1} e^{-iKn_1} \psi_{n_1}^K \times \exp \left[- \sum_{n_2} (\lambda_{n_2+n_1-n}^K b_{n_2}^\dagger - \lambda_{n_2+n_1-n}^{K*} b_{n_2}) \right] |0\rangle. \quad (\text{D12})$$

Equation (D12) can be obtained from Eq. (D5) by relabeling n as $n-n_1$, and n_1 as n . Defining the phonon part of the wave function as $|\Phi_n^K\rangle$ [the summation over n_1 in Eq. (D12)],

$$|\Phi_n^K\rangle = \sum_{n_1} e^{-iKn_1} \psi_{n_1}^K |\Lambda_{n-n_1}^K\rangle, \quad (\text{D13})$$

$|K\rangle$ is written in the compact form

$$|K\rangle = L_0^{-1/2} \sum_n e^{iKn} |\Phi_n^K\rangle B_n^\dagger |0\rangle_{ex}. \quad (\text{D14})$$

We approximate the density matrix by Eq. (42), which is well-justified in the low temperature regime (especially for intermediate and strong exciton-phonon-couplings a finite gap is formed between the one-exciton ground state and the high-lying phonon continuum). Carrying out the trace over the phonon bath, one arrives at

$$\rho_{mn} = \sum_K \langle K|K\rangle^{-1} e^{-\beta E_K} e^{iK(m-n)} \langle \Phi_n^K | \Phi_m^K \rangle, \quad (\text{D15})$$

where

$$\langle \Phi_n^K | \Phi_m^K \rangle = \sum_{n_1, n_2} e^{iK(n_1-n_2)} \psi_{n_1}^{K*} \psi_{n_2}^K \times \exp \left[L_0^{-1} \sum_q |\lambda_q^K|^2 (e^{iq(n_2-n_1)+iq(n-m)} - 1) \right]. \quad (\text{D16})$$

Noting that

$$\langle \Phi_n^K | \Phi_n^K \rangle = L_0^{-1} \langle K|K\rangle, \quad (\text{D17})$$

we have

$$\rho_{nn} = L_0^{-1}. \quad (\text{D18})$$

Also ρ_{mn} is found to be real so that

$$\rho_{mn} = \rho_{nm}. \quad (\text{D19})$$

Taking into account the translational symmetry, we may label ρ_{mn} with one index, i.e., $\rho_{m-n} = \rho_{mn}$.

We now discuss the connection between adiabatic polaron theory and variational Ansätze. Equation (49) can also be deduced using a time-dependent variational principle as soliton theory is usually implemented. Localized polaron Ansätze, such as the Davydov Ansatz,

$$\sum_n \psi_n(t) B_n^\dagger |0\rangle_{ex} \otimes \exp \left[- \sum_n (\lambda_n(t) b_n^\dagger - \lambda_n^*(t) b_n) \right] |0\rangle_{ph} \quad (\text{D20})$$

are often employed, and equations of motion are derived for the time-dependent parameters characterizing the exciton wave function and the phonon fields. Neglecting the time-derivative of the phonon fields λ_n as the adiabatic condition requires, Eq. (E8) is recovered, and the exciton wave function is found to follow Eq. (49). For large polarons where the continuum approximation is justified, the static solution for the exciton wave function again assumes the soliton profile (50). The physical picture is that the exciton creates a static lattice deformation λ_n and then become self-trapped in the potential well that is established by the deformation.

The delocalized Toyozawa Ansatz employed in this work can be obtained by applying a delocalization projection operator

$$\hat{P} = L_0^{-1} \sum_n \exp \left[in \left(K - \sum_k k B_k^\dagger B_k - \sum_q q b_q^\dagger b_q \right) \right] \quad (\text{D21})$$

to the Davydov Ansatz (D20). Within the Toyozawa Ansatz, a ‘‘locking’’ relation similar to (E8) is found for λ_n^K and ψ_n^K in the adiabatic regimes of the phase diagram for both small and large polarons,⁴⁶ although for weak exciton-phonon-coupling nonadiabaticity emerges as the one-phonon plane-wave from the background of the large adiabatic polaron as the coupling is decreased. It is worth noting that extended states yield lower energies than the localized parent states.⁷⁵ Ansatz (D5) with optimized λ_n^K and ψ_n^K , and its generalization with the replacement of $\lambda_{n_2-n}^K$ in (D5) by a two-parameter sum $\alpha_{n_2-n}^K + \beta_{n_2-n_1}^K$, constitute the most sophisticated variational wave functions applied to the Holstein Hamiltonian. We note that the delocalization procedure which transforms (D20) into (D5) preserves the locality of exciton-phonon correlations.

APPENDIX E: ADIABATIC POLARONS

In this Appendix we evaluate the reduced exciton density matrix ρ_{mn} using the adiabatic polaron model. To that end we represent the phonon Hamiltonian which enters Eq. (1) in a form:

$$H_{ph} = T_{ph} + V(\mathbf{q}), \quad (\text{E1})$$

where T_{ph} is the nuclear kinetic energy and $V(\mathbf{q})$ is the potential energy. We adopt the Born-Oppenheimer approach to the polaron problem^{60,76,77} by representing the eigenfunctions of the joint system in a form

$$\Phi = \sum_n \Psi_\alpha(n; \mathbf{q}) B_n^\dagger |0\rangle \Lambda_\alpha(\mathbf{q}), \quad (\text{E2})$$

where $\Psi_\alpha(n; \mathbf{q})$ is the α th exciton wave function with energy $E_\alpha(\mathbf{q})$. $\Lambda_\alpha(\mathbf{q})$ is an eigenfunction of the phonon effective adiabatic Hamiltonian H_α^{eff} defined as

$$H_\alpha^{eff} \equiv T_{ph} + V_\alpha^{eff}(\mathbf{q}), \quad (\text{E3})$$

with

$$V_\alpha^{eff}(\mathbf{q}) \equiv V(\mathbf{q}) + E_\alpha(\mathbf{q}). \quad (\text{E4})$$

The adiabatic ansatz for the wave functions represented by Eqs. (E2)–(E4) allows to represent the reduced exciton density matrix in a form

$$\rho_{mn} = \sum_\alpha \int d\mathbf{q} \Psi_\alpha^*(m; \mathbf{q}) \Psi_\alpha(n; \mathbf{q}) \langle \mathbf{q} | \exp(-H_\alpha^{eff}/T) | \mathbf{q} \rangle. \quad (\text{E5})$$

If the energy splitting between trapped excitons is larger than the temperature, only the $\alpha=0$ term related to the lowest exciton needs to be retained in Eq. (E5) which yields

$$\rho_{mn} = \int d\mathbf{q} \Psi^*(m; \mathbf{q}) \Psi(n; \mathbf{q}) \langle \mathbf{q} | \exp(-H^{eff}/T) | \mathbf{q} \rangle, \quad (\text{E6})$$

where the $\alpha=0$ subscript has been omitted.

If temperature is higher than the phonon frequency the phonon density matrix $\exp(-H^{eff}/T)$ can be represented in form

$$\rho_{mn} = Z^{-1} \sum_\alpha \int d\mathbf{q} \Psi_\alpha^*(m; \mathbf{q}) \Psi_\alpha(n; \mathbf{q}) \times \exp(-V_\alpha^{eff}(\mathbf{q})/T), \quad (\text{E7})$$

with the partition function $Z \equiv \int d\mathbf{q} \exp(-V^{eff}(\mathbf{q})/T)$. Equation (E7) is valid for any number of low-frequency modes coupled to molecules; q_n should then be treated as the collective bath coordinate coupled to the n th molecule^{78,79} rather than a single-mode (microscopic) coordinate.

The integral on the r.h.s. of Eq. (E7) can be computed using Monte Carlo techniques. Here to get a qualitative picture we consider a simple case when the temperature is higher than the frequencies of low-energy nuclear modes, but is still lower than the energy scale of the variation of V^{eff} itself. In this case the most important contributions to the integral in Eq. (E7) come from the vicinity of the minimum of $V^{eff}(\mathbf{q})$. The existence of a nontrivial minimum of V^{eff} in low-dimensional systems has been outlined by Rashba.³³ At the minimum of V^{eff} we have

$$q_n = g |\Psi(n)|^2 \quad (\text{E8})$$

and the exciton wave function satisfies the discrete nonlinear Schrödinger equation^{33,34,54} given by Eq. (49). When each molecule is coupled to a distribution of solvent modes, the parameter λ can be expressed in terms of the bath spectral density $C(\omega)$:⁷⁸

$$\lambda = \int_{-\infty}^{\infty} \frac{d\omega}{2\pi} \frac{C(\omega)}{\omega}. \quad (\text{E9})$$

Solutions of Eq. (49) are commonly referred to as solitons. The nonlinearity induced by the exciton-phonon coupling is the mechanism supporting the soliton excitations. For the continuum model with the solution given by Eq. (50) the energy splitting between the lowest trapped exciton and the next one is given by $\lambda^2/|J|$.³⁴ This implies that Eq. (E5) which is valid in the adiabatic limit is derived under the condition $\omega_0 \ll \lambda^2/|J|$. This equation leads to Eq. (E6) in the $T \ll \lambda^2/|J|$ limit. Equation (E7) which follows from Eq. (E6) when $T \gg \omega_0$ is hence valid when $\omega_0 \ll T \ll \lambda^2/|J|$.

Neglecting fluctuations of collective bath coordinates in the vicinity of the minimum of $V^{eff}(\mathbf{q})$ we obtain a simple expression for ρ_{mn} given by Eq. 48. Equation. (48) can also be obtained using the Toyozawa ansatz and setting the Debye-Waller factor $\langle \Lambda_n^K | \Lambda_n^K \rangle = \delta_{nn'}$, which means that in the adiabatic polaron theory $l_{DW} = 0$ (this reflects the fact that the traps related to left and right components of the density matrix have the same positions) and l_p is the only lengthscale which determines L_p .

¹R. van Grondelle, J. P. Dekker, T. Gillbro, and V. Sundström, *Biochim. Biophys. Acta* **1187**, 1 (1994).

²V. Sundström and R. van Grondelle, in *Anoxygenic Photosynthetic Bacteria*, edited by R. E. Blankenship, M. T. Madiga, and C. E. Baner (Kluwer Academic, Dordrecht, 1995), p. 349.

³S. E. Bradforth, R. Jimenez, F. von Mourik, R. van Grondelle, and G. R. Fleming, *J. Phys. Chem.* **99**, 16 179 (1995).

⁴R. Jimenez, S. R. Dikshit, S. E. Bradforth, and G. R. Fleming, *J. Phys. Chem.* **100**, 6825 (1996).

⁵H. van der Laan, Th. Schmidt, R. W. Visschers, K. J. Visscher, R. van Grondelle, and S. Völker, *Chem. Phys. Lett.* **170**, 231 (1990).

⁶N. R. S. Reddy, G. J. Small, M. Seibert, and P. Picorel, *Chem. Phys. Lett.* **181**, 391 (1991).

⁷N. R. S. Reddy, R. J. Cogdell, L. Zhao, and G. J. Small, *Photochem. Photobiol.* **57**, 35 (1993).

⁸C. De Caro, R. W. Visschers, R. van Grondelle, and S. Völker, *J. Phys. Chem.* **98**, 10 584 (1994).

⁹T. Pullerits, M. Chachisvilis, and V. Sundström, *J. Phys. Chem.* **100**, 10 787 (1996).

¹⁰T. Pullerits, M. Chachisvilis, M. R. Jones, C. N. Hunter, and V. Sundström, *Chem. Phys. Lett.* **224**, 355 (1994).

¹¹V. Nagarajan, R. G. Alden, J. C. Williams, and W. W. Parson, *Proc. Natl. Acad. Sci. USA* **93**, 13774 (1996).

¹²D. Leupold, H. Stiel, K. Teuchner, F. Nowak, W. Sandner, B. Ücker, and H. Scheer, *Phys. Rev. Lett.* **77**, 4675 (1996).

¹³T. Joo, Y. Jia, J.-Y. Yu, D. M. Jonas, and G. R. Fleming, *J. Phys. Chem.* **100**, 2399 (1996).

¹⁴R. Jimenez, F. van Mourik, and G. R. Fleming, *J. Phys. Chem.* (in press).

¹⁵D. Mobius and H. Kuhn, *Isr. J. Chem.* **18**, 375 (1979); *J. Appl. Phys.* **64**, 5318 (1988).

¹⁶D. P. Craig and T. Thirunamachandran, *Molecular Quantum Electrodynamics* (Academic, New York, 1984).

¹⁷V. M. Agranovich and O. Dubovsky, *Sov. Phys. JETP Lett.* **3**, 223 (1966).

¹⁸J. Grad, G. Hernandez, and S. Mukamel, *Phys. Rev. A* **37** 3838 (1988); A. I. Zaitsev, V. A. Malyshev, and E. D. Trifonov, *Sov. Phys. JETP* **57**, 275 (1983).

¹⁹Y. C. Lee and R. S. Lee, *Phys. Rev. B* **10**, 344 (1974); V. Sundström, T. Gillbro, R. A. Gadonas, and A. Piskarskas, *J. Chem. Phys.* **89**, 2754 (1988).

²⁰F. C. Spano and S. Mukamel, *J. Chem. Phys.* **91**, 683 (1989).

²¹V. Sundström, T. Gillbro, R. A. Gadonas, and A. Piskarskas, *J. Chem. Phys.* **89**, 2754 (1988).

- ²²R. Monshouwer, M. Abrahamsson, F. van Mourik, and R. van Grondelle, *J. Phys. Chem.* (in press).
- ²³F. C. Spano, Kuklinski, and S. Mukamel, *Phys. Rev. Lett.* **65**, 211 (1990); *J. Chem. Phys.* **94**, 7543 (1991).
- ²⁴V. A. Malyshev, *Opt. Spectrosc.* **71**, 505 (1991); *J. Lumin.* **55**, 225 (1993).
- ²⁵H. Fidder, J. Knoester, and D. A. Wiersma, *Chem. Phys. Lett.* **171**, 529 (1990).
- ²⁶Y. R. Kim, M. Lee, J. R. G. Thorne, R. M. Hochstrasser, and Y. M. Zeigler, *Chem. Phys. Lett.* **145**, 75 (1988); J. R. G. Thorne, R. M. Hochstrasser, and Y. M. Zeigler, *J. Phys. Chem.* **92**, 4275 (1988).
- ²⁷J. R. Durrant, J. Knoester, and D. A. Wiersma, *Chem. Phys. Lett.* **222**, 450 (1994).
- ²⁸A. A. Muentner, D. V. Brumbaugh, J. Apolito, L. A. Horn, F. C. Spano, and S. Mukamel, *J. Chem. Phys.* **96**, 2784 (1992); J. M. Lanzafame, A. A. Muentner, and D. V. Brumbaugh, *Chem. Phys.* **210**, 79 (1996).
- ²⁹S. de Boer and D. A. Wiersma, *Chem. Phys. Lett.* **165**, 45 (1990).
- ³⁰H.-P. Dorn and A. Müller, *Chem. Phys. Lett.* **130**, 426 (1986).
- ³¹N. F. Mott and W. D. Twose, *Adv. Phys.* **10**, 107 (1961); V. L. Berezinskii, *Zh. Eksp. Teor. Fiz.* **65**, 1251 (1973).
- ³²N. Wang, A. Muentner, and S. Mukamel, *J. Chem. Phys.* **99**, 3604 (1993); N. Wang, V. Chernyak, and S. Mukamel, *Phys. Rev. B* **50**, 5609 (1994).
- ³³E. I. Rashba, *Opt. Spektrosk.* **2**, 75 (1957); *ibid.* **2**, 88 (1957).
- ³⁴T. Holstein, *Ann. Phys. (N.Y.)* **8**, 325, 343 (1959).
- ³⁵In fact, for the present results to hold, suffice it to assume that the resulting coherence size is small compared with the optical wavelength, regardless of the physical size, which is typically the case.
- ³⁶E. N. Economou, *Green's Functions in Quantum Physics* (Springer, New York, 1983).
- ³⁷O. Dubovsky and S. Mukamel, *J. Chem. Phys.* **95**, 7828 (1991).
- ³⁸S. Mukamel, in *Molecular Nonlinear Optics*, edited by J. Zyss, (Academic, New York, 1994).
- ³⁹S. Mukamel and H. X. Wang, *Phys. Rev. Lett.* **69**, 65 (1992); S. Mukamel and H. X. Wang, in *Optics of Semiconductor Nanostructures*, edited by F. Henneberger, S. Schmitt-Rink and E. O. Göbel, (Akademie Verlag, Berlin, 1993); S. Mukamel, A. Takahashi, H. X. Wang, and G. Chen, *Science* **266**, 250 (1994).
- ⁴⁰S. Yokojima, T. Meier, and S. Mukamel, *J. Chem. Phys.* **106**, 3837 (1997).
- ⁴¹G. McDermott, S. M. Prince, A. A. Freer, A. M. Hawthornthwaite-Lawless, M. Z. Papiz, R. J. Cogdell, and N. W. Isaacs, *Nature* **374**, 517 (1995).
- ⁴²K. Sauer, R. J. Cogdell, S. M. Prince, A. A. Freer, N. W. Isaacs, and H. Scheer, *Photochem. Photobiol.* **64**, 564 (1996).
- ⁴³R. Zwanzig, *Lect. Theor. Phys.* **3**, 106 (1961); *Physica* **30**, 1109 (1964); H. Mori, *Prog. Theor. Phys.* **33**, 423; **3**, 399 (1965).
- ⁴⁴A. G. Redfield, *Adv. Magn. Reson.* **1**, 1 (1965).
- ⁴⁵R. W. Munn and R. Silbey, *J. Chem. Phys.* **83**, 1843 (1985).
- ⁴⁶Y. Zhao, D. W. Brown, and K. Lindenberg, *J. Chem. Phys.* **100**, 2335 (1994); *ibid.* **106**, 2728 (1996).
- ⁴⁷A. Matsui and K. Mizuno, *Exciton dynamics in organic molecular crystals*, 5th Intern. Conf. on Excited States in Solids, Lyon (1985).
- ⁴⁸D. Emin, *Adv. Phys.* **22**, 57 (1973).
- ⁴⁹G. D. Mahan, *Many-Particle Physics* (Plenum, New York, 1981).
- ⁵⁰Y. Toyozawa, *Prog. Theor. Phys.* **26**, 29 (1961).
- ⁵¹S. I. Pekar, *Untersuchungen über die Elektronentheorie der Kristalle* (Akademie-Verlag, Berlin, 1954).
- ⁵²H. Fröhlich, *Proc. R. Soc. London, Ser. A* **160**, 230 (1937); *Adv. Phys.* **3**, 325 (1954).
- ⁵³M. Born and J. R. Oppenheimer, *Ann. Phys. (Leipzig)* **87**, 457 (1927).
- ⁵⁴G. Venzl and S. F. Fischer, *J. Chem. Phys.* **81**, 6090 (1984).
- ⁵⁵E. I. Rashba, *Synth. Met.* **64**, 255 (1994).
- ⁵⁶G. Whitfield and R. D. Puff, *Phys. Lett.* **10**, 9 (1964); *Phys. Rev.* **139**, A335 (1965).
- ⁵⁷K. Cho and Y. Toyozawa, *J. Phys. Soc. Jpn.* **30**, 1555 (1971).
- ⁵⁸H. Sumi, *J. Phys. Soc. Jpn.* **36**, 770 (1974).
- ⁵⁹A. V. Sherman, *Phys. Status Solidi (B)* **141**, 151 (1987).
- ⁶⁰V. Broude, E. I. Rashba, and E. F. Sheka, *Spectroscopy of Molecular Excitons* (Springer-Berlin, 1985).
- ⁶¹T. Meier, V. Chernyak, and S. Mukamel, *J. Phys. Chem.* (in press).
- ⁶²M. van Burgel, D. A. Wiersma, and K. Duppen, *J. Chem. Phys.* **102**, 20 (1995).
- ⁶³H. Fidder, Ph.D. Thesis, Rijksuniversiteit Groningen, Netherlands, 1993.
- ⁶⁴J. A. Leegwater, *J. Phys. Chem.* **100**, 14403 (1996).
- ⁶⁵A. A. Abrikosov, L. P. Gorkov, and I. E. Dzyaloshinski, *Methods of Quantum Field Theory in Statistical Physics* (1963).
- ⁶⁶N. Mott, *Metal-Insulator Transitions* (Taylor and Francis, London, 1974).
- ⁶⁷We note that as shown in Ref. 61 the shift in the pump-probe signal is not a direct evidence of exciton localization or self-trapping, for weak-exciton-phonon coupling it can originate from phonon-induced exciton dephasing. In this case the shift has a collective nature reflecting statistical properties of exciton states coupled to phonons.
- ⁶⁸R. Silbey and R. W. Munn, *J. Chem. Phys.* **72**, 2763 (1980).
- ⁶⁹R. W. Munn and R. Silbey, *J. Chem. Phys.* **83**, 1854 (1985).
- ⁷⁰W. T. Pollard, A. K. Felts, and R. A. Friesner, *Adv. Chem. Phys.* **XCIII**, 77 (1996), edited by I. Prigogine and S. A. Rice.
- ⁷¹H. Haken and G. Strobl, *Z. Phys.* **262**, 135 (1973).
- ⁷²R. F. Loring and S. Mukamel, *J. Chem. Phys.* **85**, 1950 (1986); R. F. Loring, M. Sparpaglione, and S. Mukamel, *ibid.* **86**, 2249 (1987); S. Mukamel, D. S. Franchi, and R. F. Loring, *Chem. Phys.* **128**, 99 (1988).
- ⁷³V. M. Kenkre and P. Reinecker, *Exciton Dynamics in Molecular Crystals*, Springer Tracts in Modern Physics (Springer, Berlin, 1982).
- ⁷⁴D. Feinberg, S. Ciuchi, and F. de Pasquale, *Int. J. Mod. Phys. B* **4**, 1317 (1990).
- ⁷⁵V. Čapek and D. Krausová, *Czech. J. Phys. B* **37**, 1201 (1987).
- ⁷⁶P. B. Shaw and G. Whitfield, *Phys. Rev. B* **17**, 1495 (1978).
- ⁷⁷L. A. Turkevich and T. D. Holstein, *Phys. Rev. B* **35**, 7474 (1987).
- ⁷⁸S. Mukamel, *Principles of Nonlinear Optical Spectroscopy* (Oxford, New York, 1995).
- ⁷⁹V. Chernyak and S. Mukamel, *J. Chem. Phys.* **105**, 4565 (1996).